國立臺灣大學工學院高分子科學與工程研究所

碩士論文

Graduate Institute of Polymer Science and Engineering

College of Engineering

National Taiwan University

Master's Thesis

以拉格朗齊模擬及三維列印輔助閥件設計

Design of Valves with the Lagrangian Simulation and 3D
Printing

胡志佑

Chih-Yu Hu

指導教授：童世煌教授

Advisor: Shih-Huang Tung, Ph.D.

中華民國 112 年 9 月

September, 2023

國立臺灣大學碩士學位論文

口試委員會審定書

以拉格朗齊模擬及三維列印輔助閥件設計

Design of Valve with the Lagrangian Simulation. and 3D Printing

本論文係胡志佑君（學號 r09549025）在國立臺灣大學高分子科學與工程學研究所完成之碩士學位論文，於民國 112 年 09 月 11 日承下列考試委員審查通過及口試及格，特此證明

口試委員：

_____ （簽名）

（指導教授）

_____   _____
胡哲嘉

_____   _____

系主任、所長 _____ （簽名）

I

II

中文摘要

　　無論在哪裡應用閥及管件，它們都面臨著顆粒耐受性的主要問題。克服顆粒對閥行為的影響的各種方法是已知的。在輸送系統的情況下，顆粒的累積直接影響其可靠性，尤其是考慮長期應用時。半導體的大量使用酸鹼液，不管是在水系統以及化學系統，皆會有顆粒堆積在轉彎處及流速較慢處，對於一個大系統，希望流過的流體都有充分利用到，並能順利通過每一個管路及閥件，也確保管件不會因為顆粒堆積造成管件使用年限下降。

　　早期在進行研究時,以理論推導為主要實驗之方式,而數值模擬則因受限於電腦的運算速度,能應用的範圍受到許多限制,直到近年來由於電腦技術的快速發展,在運算能量的大幅提升的情況下，計算效能與可處理問題之複雜度皆已達到符合實際應用之水準使得過去需要耗用大量資源，甚至難以進行的模擬都成為可應用之對象，計算流體力學於管路之模擬案例逐年增加。

　　本研究成功使用 COMSOL 軟體建立三種不同閥件模型並進行流體模擬及粒子分析，在流體模擬方面，針對閥中的流變模式，採用模擬牛頓流體的 Navier-Stokes 方程可以模擬閥的流變行為，考慮顆粒碰撞阻力/紊流力與剪應變率平方成正相關，將顆粒碰撞阻力/紊流力體積力加入 Navier-Stokes 方程式。我們使用水以及 IPA 兩種不同流體進行流體分析，另外，本研究於粒子分析中，使用 Euler-Lagrangian Simulation 之分析，並與實驗數據進行比較，結果顯示此方法與實驗數據相比，誤差約為 3%且最佳流速為 0.39m/s，且歸納出在閥件中設計

45 度斜板，以及在彎管處設計 r=0.75mm 之導角有利最少粒子堆積。

　　本研究檢討上述的模擬方法可以合理的模擬顆粒在閥件中的堆積行為，並探討不同因數與模式參數值如何影響顆粒的堆積行為。最後透過 3D 列印的方法列印出所設計之閥件。
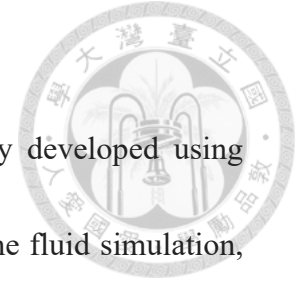
關鍵字：3D 模擬、3D 列印、熱熔融層積、光固化成型、液體閥

IV

Abstract

Wherever valves and fittings are applied, they face the major problem of particle tolerance. Various methods to overcome the effects of particles on valve behavior are known. In the case of conveyor systems, the accumulation of particles has a direct impact on their reliability, especially when long-term applications are considered. In the case of semiconductors, which are used in large quantities in acids and alkalis, both in aqueous systems and chemical systems, there is a build-up of particles at bends and slow flow points. For a large system, it is desirable that the flow is fully utilized and passes smoothly through each line and valve fitting, and that the fittings do not suffer from a decline in service life due to particle build-up.

Early in the research, theoretical derivation as the main experimental approach, and numerical simulation is limited by the computer's computing speed, can be applied to the scope of many limitations, until recent years due to the rapid development of computer technology, in the case of a substantial increase in computing energy, computational performance and the complexity of the problems that can be dealt with have reached a level consistent with the actual application of the standard so that in the past need to spend a lot of resources, and even difficult to carry out the simulation have become applicable. Simulations that used to be resource-intensive or even difficult to perform have become applicable, and the number of computational fluid dynamics

simulations on pipelines is increasing year by year.

In this study, three different valve models were successfully developed using COMSOL software for fluid simulation and particle analysis. In the fluid simulation, the Navier-Stokes equations, which are used to simulate Newtonian fluids, were used to simulate the rheological behavior of the valve for the rheological modes of the valve, and the particle collision resistance/turbulence force was added into the Navier-Stokes equations to consider that it is positively correlated to the square of shear rate of change, and the particle collision resistance/turbulence force is added into the Navier-Stokes equations. The particle collision resistance/turbulence force is added to the Navier-Stokes equation. Two different fluids, water and IPA, were used for the fluid analysis. In addition, the Euler-Lagraigian Simulation was used for the particle analysis and compared with the experimental data, and the results showed that the error of this method was about 3% and the optimal flow velocity was 0.39 m/s compared with the experimental data.

Keywords: Liquid valve, COMSOL Multiphysics, 3D simulation, 3D printing, FDM, SLA

CONTENTS

LIST OF FIGURES

X

LIST OF TABLES

Chapter 1 INTRODUCTION

With the progress of the times, science and technology are changing with each passing day., the demand for product purity is getting higher and higher, therefore, the filtration of nanoparticles has become the focus of the industry, and the moti capture technology of nanoparticles has also become an important topic in the academic world. By understanding the motion patterns of the particles, we can further understand the principles of film fouling and the particle trapping patterns. This information can be used to fundamentally assist in the design of membrane materials, to solve fouling problems, and to optimize the particle trapping effect of thin films.

In semiconductor manufacturing, acid and alkali fluids are frequently employed in both water and chemical systems. As a result, particles tend to accumulate in bends and areas with slow-flow. In the case of large systems, the goal is to maximize fluid flow efficiency, ensuring it smoothly traverses each pipe and valve while also safeguarding fittings against premature wear caused by particle buildup.

In the early days of research, theoretical derivation was the main experimental method, and numerical simulation was limited by the speed of computer computation, and the scope of application was limited, until recent years due to the rapid development of computer technology, in the case of computing energy has increased significantly, the computational efficiency and complexity of the problems can be dealt with have

reached a level that meets the standard of practical application, so that the simulation of the past need to use a lot of resources, and even difficult to carry out have become applicable. Simulations that used to be resource-intensive or even difficult to perform have become applicable, and the number of computational fluid dynamics simulations on pipelines is increasing year by year.

In this study, three different valve models were successfully developed using COMSOL software for fluid simulation and particle analysis. In the fluid simulation, the Navier-Stokes equations, which are used to simulate Newtonian fluids, were used to simulate the rheological behavior of the valve for the rheological modes of the valve, and the particle collision resistance/turbulence force was added into the Navier-Stokes equations to consider that it is positively correlated to the square of shear rate of change, and the particle collision resistance is added into the Navier-Stokes equations. The particle collision resistance/turbulence force is added to the Navier-Stokes equation. Two different fluids, water and IPA, were used for the fluid analysis. In addition, the Euler-Euler Simulation was used for the particle analysis and compared with the experimental data, and the results showed that the error of this method was about 3% and the optimal flow velocity was 0.39 m/s compared with the experimental data.

2

Chapter 2 Literature Review

2.1 Particle Flow Patterns in Valve

Particles in the valve parts for the solid particles and liquid mixed fluid,solid and liquid interaction. The transfer process, including viscous force and turbulence between the slurry strength and friction between the particles and collision force, and the strength of these factors in addition to the composition of the particle.

The strength of these factors is not only related to the composition of the particles, but also to their flow rate, making the particle flow situation more complex. In order to explain the flow situation, it is necessary to have an appropriate rheological model to investigate the relationship between the shear stress, τ and the shear strain rate, $\dot{\gamma}(=du/dz)$ inside the particles and the fluid, and to find out the rheological characteristics of the particles. So far, many rheological models have been proposed by many scholars. In the following, the rheological modes that are commonly used to characterize the particle flow are introduced:

4
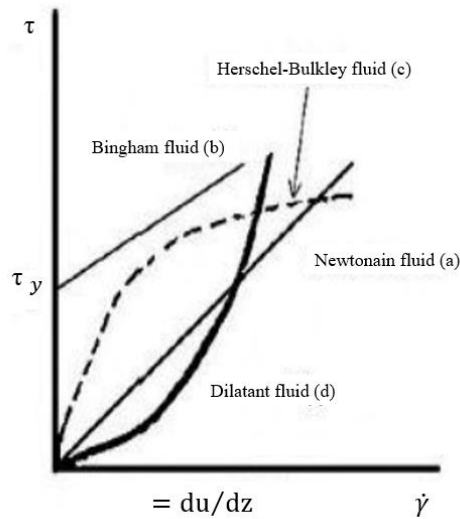
Figure 2.1 Commonly used models of particle rheology [1]

2.1.1 Newtonian Fluid Model

This model is the earliest used in the particles of the rheological model, such as Figure 2.1 (a) straight line, Newtonian fluid means that the viscosity coefficient of the fluid at a constant temperature for a certain value, and viscosity coefficient is not affected by the concentration and flow rate and other factors. The rheological equation is as follows:

$$\tau = \mu\dot{\gamma} \tag{2.1}$$

where: μ: viscosity coefficient, τ: shear stress, $\dot{\gamma} = \frac{du}{dz}$ shear strain rate.

This model is more suitable for particle-laden waters with low particle contents (Cv<20%), and is not suitable for analyzing particle flows with higher particle contents

5
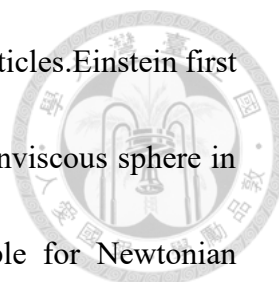
because it cannot describe the cohesion and friction between the particles. Einstein first proposed a method for calculating the viscosity coefficient of a nonviscous sphere in Newtonian fluids in 1906, and the method proved to be suitable for Newtonian representation of fluids with a volume concentration (C_v) of less than 2%. This method has been proven to be suitable for Newtonian fluids with volume concentration (C_v) less than 2%. The relationship between the concentration and volume concentration is given in the following equation:

$$\mu = \mu_o \left(1 + 2.5C_v \right) \tag{2.2}$$

Where μ_o : viscosity coefficient of water, about 10^{-3} (Pa * s)

C_v: volume concentration, which is physically defined as:

$$C_v = \frac{\rho_m - \rho_w}{\rho_s - \rho_w} = \frac{\rho_m - \rho_w}{G_s \rho_w - \rho_w} = \frac{1}{1 + G_s W_c} \tag{2.3}$$

ρ_m: particle flow density

ρ_w: water density

ρ_s: particle solid density

G_s: specific gravity of particles in solid state

W_c (%): water content

In 1952, Roscoe proposed two equations for a water body containing homogeneous particles (Eq. (2.4)) and non-homogeneous particles (Eq. (2.5)):

$$\mu = \mu_o \left(1 - 1.35 \times C_v \right)^{-2.5} \tag{2.4}$$

$$\mu = \mu_o \left(1 - C_v \right)^{-2.5} \tag{2.5}$$

6
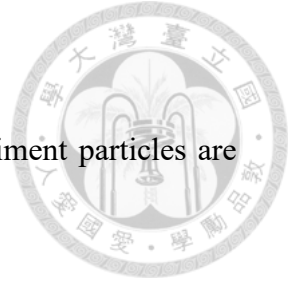
Where,

C_{vm}: the maximum limit concentration of the particles, in the sediment particles are spherical, C_{vm} is about 0.74, B value 2.5.

Bagnold (1954), based on the experimental results, assumed that when the fluid is viscous, the effect of the presence of particles on the viscosity is shown in the following equation:

$$\mu = 2.2\ 5\mu_o\lambda^{1.5} \tag{2.6}$$

where is the linear concentration, and the relationship between it and the particle concentration is:

$$\lambda = [(\frac{C_{vm}}{C_v})^{\frac{1}{3}} - 1]^{-1} \tag{2.7}$$

where C_{vm} is the maximum limit concentration of particles.

2.1.2 Frictional Rheological Model

The basin of a granular flow with strong inter-particle friction effect is closer to the friction mode. Assuming that the pore water content in the granular flow is very low, the sliding friction between particles in this basin is the mode of momentum transfer between particles in the granular flow because the particles move slowly and are closely spaced apart, thus the basin is called a friction regime. According to Coulomb's friction theory, the shear and forward forces in any cross-section of a friction domain are given

7

By the flowing

$$\tau = c + \sigma_n \tan \varphi_c \qquad (2.8)$$
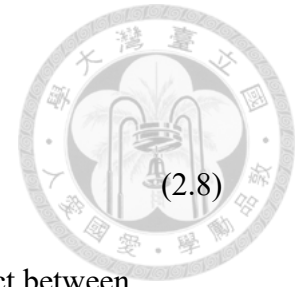
τ: shear force, σn: internal normal force generated by mutual contact between

particles in the shear surface

c: cohesive strength

φ_c: internal friction angle of the particles

which generally varies with the volume concentration C_{vm}, but is usually regarded as

a constant value.

2.1.3 Bingham Rheology Model

The Bingham model is a rheological relationship proposed by Bingham and Green

in 1920, as shown in the (b) line in Fig. 2.1, also known as the viscoplastic model

(Visco-Plastic model), which contains a Bingham Yield stress, and the shear stress on

the fluid needs to be greater than the Bingham Yield stress for the shear stress to have

a rate of change, and the equation is as follows:

$$\tau = \tau_B + \mu_B \dot{\gamma} \qquad (2.9)$$

Where τ_B is the Bingham yield stress and μ_B is the Bingham viscosity coefficient, these

two parameters are affected by the particle content, particle size distribution,

temperature, acidity and alkalinity of the particle stream (Johnson, 1970, O'Brien et al.,

1988) [1].
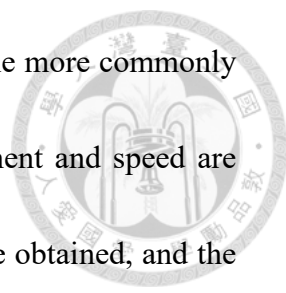
The formation of the Bingham yield stress τ_B is mainly due to the flocculation structure of the viscous particles and the frictional resistance between the particles. In the case of granular flow, the flocculating structure of the particles is the main cause of the τ_B yield stress, and Johnson (1965) expressed the yield stress in terms of frictional modes from experimental and field observations of granular flow, frictional modes are cohesive and internally oriented, where the frictional force is directly proportional to the oriented stress acting on the shear surface. The Coulomb-Viscous model proposed by Johnson is as follows:

$$\tau = c + \sigma_n \tan \varphi_c + \mu_B \dot{\gamma} \tag{2.10}$$

The first two items on the right side of the equal sign are the parts of the buckling stress, which must be exceeded if the particle flow starts. τ_B and μ_B are not constant values, but vary with the volume concentration of the particle flow, the shape of the particles, the particle nature, the particle size distribution, the temperature, etc.

The Bingham coefficient of viscosity (μ_B) is comparable to the coefficient of viscosity of Newtonian fluids, and the Bingham coefficient of viscosity can be calculated in the same way as the coefficient of viscosity of Newtonian fluids. However, most of the Bingham coefficients are obtained from indoor test methods. Generally, the soil and rock slurry portion of the sample is taken, and the maximum particle size of the sample

9
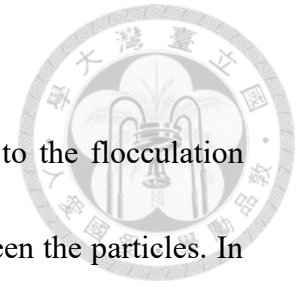
is determined according to the limitations of the test instrument. The more commonly

used method is the rotational rheometer: during the test, the moment and speed are

measured, the wall shear force and the apparent shear strain rate are obtained, and the

Bingham yield stress and the Bingham coefficient of viscosity and hysteresis are

obtained by regression analysis. Although the Bingham model can describe the flow

behavior of particulate flow, it cannot completely describe the flow behavior of coarse

particles because the Bingham model does not include the discrete and turbulent forces

generated by the collision of coarse particles. However, it can be approximated by the

Bingham model if it is assumed that the discretization forces due to collision of coarse

particles are negligible. Wang (2000) used two identical experimental samples with the

same total volume concentration (i.e., volume concentration with all particle sizes, i.e.,

C_v). One was a pure fine-grained particulate stream, and the other was a particulate

stream containing a mixture of coarse and fine particles. In both cases, the Bingham

yield stress and Bingham coefficient of viscosity were measured using a Brookfield

DV-III horizontal rotational rheometer. The mixed particulate streams containing coarse

and fine particles were then separated into pure coarse particulate volume concentration

(C_{vg}) and pure fine particulate volume concentration (C_{vf}), using a 2 mm particle size

boundary. The difference between the measured yield stress and coefficient of viscosity

of the experimental samples containing a mixture of coarse and fine particles is obtained
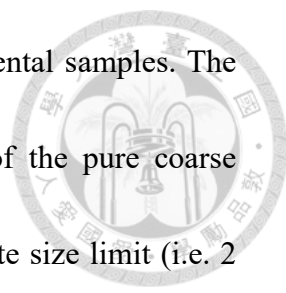
by subtracting the portion of pure fine particles from the experimental samples. The difference was then regressed on the volumetric concentration of the pure coarse particulate, the coarse particulate size and the coarse/fine particulate size limit (i.e. 2 mm) to derive the parametric equation. Finally, by adding the original equations for the yield stress and coefficient of viscosity of the pure fine particles to the regression equation for the coarse particles [2], an equation for the Bingham rheological pattern of the coarse particles is obtained. The conceptual diagram of the whole experiment is shown in Figure 2.2.
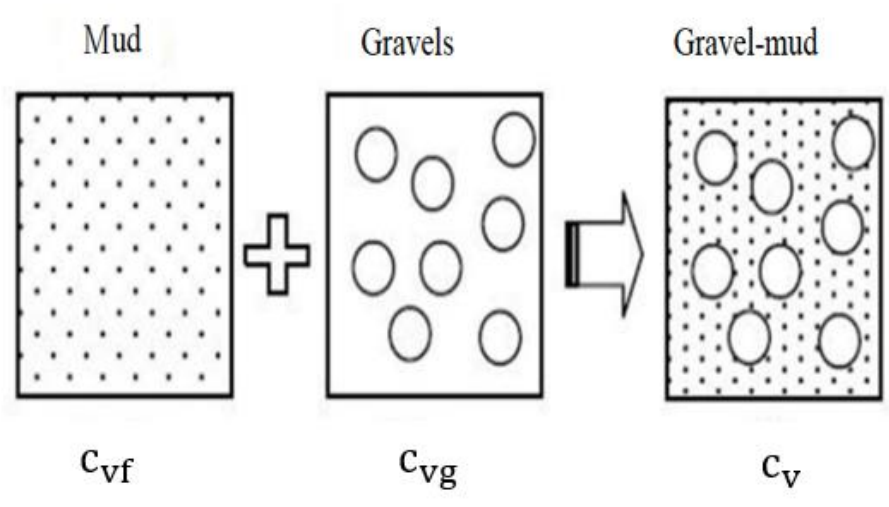
Figure 2.2 The conceptual diagram of the whole experiment

Note: Coarse particle concentration

C_{vg} = Coarse particle volume Fine particle volume + Water volume + Coarse particle volume (2.11)

Fine particle concentration C_{vf} = Coarse particle volume Fine particle volume + Water

11

volume + Coarse particle volume   (2.12)

According to the experimental results obtained by C.Y. Wang (2000), the addition of

coarse particles to fine particle slurries can slightly increase the Bingham yield stress

and the Bingham hysteresis coefficient, but the degree of increase in the Bingham yield

stress is more than that of the Bingham hysteresis coefficient.

Normally for particle flow flume experiments and numerical simulations, if the

Bingham rheological model is to be used, the Bingham Falling Stress and Bingham

Viscosity Coefficient

If the Bingham rheological model is to be used, the regression of the Bingham yield

stress τ_B and the Bingham hysteresis coefficient μ_B on the volume concentration C_v

needs to be investigated to represent the material properties of the geotechnical flow,

Eq. The regression of the Bingham yield stress τ_B and the Bingham hysteresis

coefficient μ_B on the volume concentration C_v and the regression coefficient of

Bingham viscosity μ_B show a natural logarithmic relationship with the volume

concentration C_v, and their regression equations are as follows:

$$\tau_y = \alpha_1 e^{\beta_1 C_v}$$ (2.13)

$$\mu_B = \alpha_2 e^{\beta_1 C_v}$$ (2.14)

For Eq. (2.14), in Figure (2.3), the experimental results of volume concentration C

versus Bingham viscosity coefficient μ_B are plotted in the experimental results from the

12

previous experiments using the Bingham model as the main flow channel, and the regression of μ_B for each value of C in the upper part of Fig. 2.3 is almost the same as that in Eq. (2.14). This regression calculation was later used to estimate the relationship of volume concentration on the yield stress and viscosity coefficient in the binomial rheological model proposed by O'Brien et al. (1985).
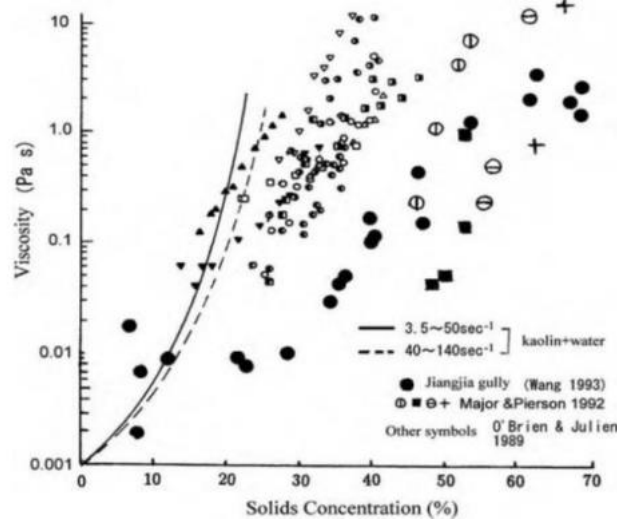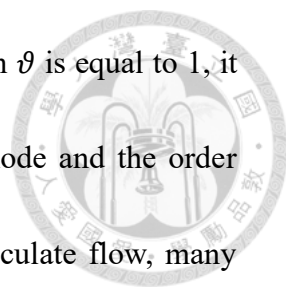
Figure 2.3 Relationship between viscosity coefficient and volume concentration of

Bingham, based on Bingham fluid [1]

2.1.4 Herschel-Bulkley Model

Herschel-Bulkley (1925) proposed that this rheological model, as shown in curve

(c) of Fig. 2-1 (the case of $\vartheta < 1$), belongs to the yield power law model with reduced

stress.

$$\tau = \tau_{HB} + \mu_{HB}\dot{\gamma}^{\vartheta} \tag{2.15}$$

From the above equation, when the shear force is larger than the yield stress τ_{HB} and ϑ

13

is not 1, the streamline curve is no longer straight but curved. When ϑ is equal to 1, it is the Bingham mode, which is a combination of the Bingham mode and the order theorem mode, and is therefore widely used. In the study of particulate flow, many researchers have adopted this rheological model to characterize the rheological properties of particulate fluids. This model is more complicated to analyze because it has three unknown parameters, but the advantage is that it is widely used and suitable for granular fluids with buckling stress and nonlinear rheology. In order to solve the problem that it is not easy to analyze with many parameters, Coussot et al. (1995) suggested that the value of ϑ in the granular fluid is a certain value, and the experimental value of ϑ is about 1.5 times the value of ϑ. (1995) considered the ϑ value in granular fluid to be a certain value, and the experimental ϑ value is about 1/3, but the ϑ values obtained by other researchers are not necessarily close to this value. Wang Zixian (2007) compiled a list of the ϑ ranges of the Herschel-Bulkly model and the relevant conditions for the Herschel-Bulkly model in Table 2.1. In addition, the Herschel-Bulkly model shares the same problem with the order theorem model, i.e., when the ϑ value is not equal to "1", μ_HB can not be defined by viscosity coefficient, but should be defined by the fluid consistency index or fluid behavior index instead. The units should not be viscosity coefficients, because they are also in the order of a power . The main purpose of the rheological model for particulate flow is that the overestimation of the yielding

14
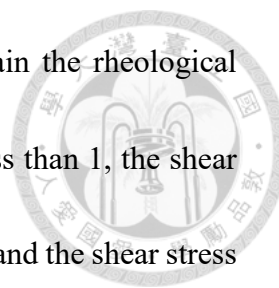
stress can easily occur when the Bingham model is used to explain the rheological

relationship of particulate flow. In the Hirschsprung model, at ϑ less than 1, the shear

strain rate is small ($<10s^{-1}$)), the shear strain rate decreases to zero, and the shear stress

decreases more than that of the Bingham flow. The shear stress τ_{HB} of the Hirschsprung

mode is smaller than that of the Bingham mode.

Coussot (1994) noted that particles with particle size less than 40 μm accounted for

more than 10% of the particle size fraction of the granular flow, whose rheological

behavior approximated the Hirschbrey pattern.

Table 2.1 The Herschel-Bulkley model proposed by the researcher ϑ-value range

Researcher	Value range	Particle Volume Concentration	Shear rate range
Coussot and Piau (1994)	0.22~0.363	15% < Cv < 41%	$0 < \frac{du}{dz} < 50s^{-1}$
Coussot and Piau (1995a)	0.33	38% < Cv < 43%	$0 < \frac{du}{dz} < 100s^{-1}$
Martino (2003)	1.66~1.85	61% < Cv < 80%	$0 < \frac{du}{dz} < 100s^{-1}$
Malet et al. (2003)	0.25 ~ 0.4	30% < Cv < 60%	$0 < \frac{du}{dz} < 250s^{-1}$
Schatzmann et al. (2003)	0.33 ~ 0.5	22.5% < Cv < 30%	$0 < \frac{du}{dz} < 100s^{-1}$

2.1.5 Collision/Dilatant Model

The collision mode is mainly applicable to the case where the inter-particle collision effect is more obvious, which is the case of the power law model with ϑ value of 2, as shown in the curve (d) of Fig. 2.1. In this type of basin, the particles flow at a certain distance, the particle deformation speed is relatively fast, and the contact time between particles is very short, so the collision between particles is the main source of momentum conversion, which is different from the sliding friction of the friction model. This basin is called collision basin [9], fully dynamic regime, or grain-inertia regime, which was first proposed by Bagnold (1954), and is also known as Dilatant model or Dispersive model. This model is also known as Dilatant model or Dispersive model in the following form:

$$\tau = P_d = \mu_d(\dot{\gamma})^2 \tag{2.16}$$

The parameter μ_d is related to the particle concentration and particle size distribution, which is defined as the consistency index. The experimental results of Bagnold (1954) show that $\mu_d = (\alpha_i \cos \alpha_i)\rho_s d_s \lambda^2$, where λ is the linear concentration, which is defined as:

$$\lambda = [(\frac{C_b}{C_v})^{\frac{1}{3}} - 1]^{-1} \tag{2.17}$$

C_v: volume concentration

C_b: Maximum volume concentration of particles in static contact.

16

Bagnold (1954) also proposed the theory of discrete stress of particles, and the

obtained discrete stress of particles and its shear stress are:

$$P_d=(\alpha_i \cos \alpha_i)\, \rho_s d_s \lambda^2 (\dot{\gamma})^2 \qquad (2.18)$$

$$\tau_d = P_d \tan \alpha_i=(\alpha_i \sin \alpha_i)\rho_s d_p \lambda^2 (\dot{\gamma})^2 \qquad (2\text{-}19)$$

In the above two equations, ρ_s is the density of the particles in the granule, dp is the

particle size of the granule, α_i is the angle between the direction of the discrete stress

of the granule and the perpendicular line (z-axis), and ai is the coefficient of granule

motion. As for the coefficient of particle motion α_i, it is usually the value used in

experimental results, which is considered to be 0.042 by Bagnold, between 0.3 and 0.5

by Takahashi, and 0.0087 by Julien and Lan (1991).

Takahashi (1991) defined stony debris flow according to Bagnold (1954) and Takahashi

(1978), and the sub-bed shear stress was assumed to be resistance stress (τ_{resist}), and

Bagnold (1954) and Takahashi (1978) defined the sub-bed shear stress as τ_{resist}.

Bagnold (1954) defined the sum of shear stress (collision stress, τ_{colli}) generated by

particle collision:

$$\tau=\tau_{resist}+\tau_{colli}=(\rho_s - \rho_m)ghC_v * \cos \theta * \tan \varphi_c+\rho_d f_s U \qquad (2.20)$$

C_v : Volume concentration

h: Flow depth

ρ_m: Density of the fluid fraction of particles

17

ρ_s: Density of the solid fraction of particles

θ: Slope of flow channel

ρ_d: Overall particle flow density($\rho_d = C_{vg} * \rho_s +(1 -C_{vg}) * \rho_m$)

c: Friction angle of particles

U: average flow velocity in the cross section (m/sec)

fs: friction coefficient generated by particle collision on the flow velocity

$(fs = \frac{25(\alpha_i \sin \varphi)\rho_s d_p \lambda^2}{4\rho_d} (\frac{d_p}{h})^2)$

Tsujimoto et al. (1997) have derived the collision stress (τ_s), particle repulsive pressure

(c) and particle kinetic stress (τ_k) from the collision and motion of particles in a

particle flow. c), particle repulsive pressure,c and particle kinetic stress (τ_k) are derived.

The schematic diagram of the collision between particles is shown in Figure 2.4
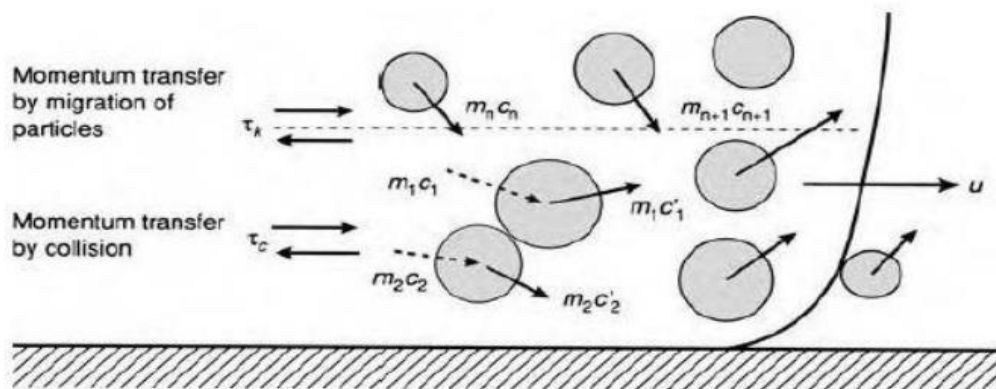
Figure 2.4 Stress relationship between particles in a high-speed particle flow [1]

In Tsujimoto et al. (1997), the collision shear stress, τ_c, and the pressure, P_c,

generated by repulsion between particles were obtained by using the stress tensor

generated by volume division of the difference in momentum at each point on the

18

surface of a single particle before and after the collision of two particles:

$$p_c = 2\rho_s {C_v}^2 g_o (1+e) \tag{2.21}$$

$$\tau_c = \frac{4}{5}\rho_s (C_v)^2 g_o (1+e) \, d_p \sqrt{\frac{T}{\pi}}(\dot{\gamma}) \tag{2.22}$$
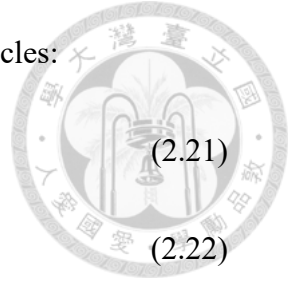
In the above two equations:

T: temperature

e: collision recovery coefficient (usually about 0.8)

ρ_s : density of the particles

d_p: particle diameter size

C_v: volume concentration

g_o: radial distribution function (physically defined as λ+1)

λ: linear concentration, as shown in equation (2.17).

Tsujimoto et al. (1997) used Gidaspow's (1994) Mixing length theory in fluid mechanics to describe the kinetic stress that occurs in the turbulent flow of particles moving in an expanding fluid (this turbulence is only between particles and particles, not between particles and the fluid bed). The kinetic stress is defined in terms of the Gaussian distribution function f The velocity distribution of the particle motion is first described by the Gaussian distribution function f_p :

$$f_p = \frac{n}{2\pi T^{\frac{3}{2}}}\exp[\frac{(C_t)^2}{2T}] \tag{2.23}$$

The average turbulent velocity $\langle Ct \rangle$ produced by the flow of all particles:

19

$$<C_t>=\frac{1}{2\pi T^{\frac{3}{2}}}\int_0^\infty C_t \exp[\frac{(C_t)^2}{2T}]dC_t=\sqrt{\frac{8T}{\pi}} \qquad (2.24)$$

The physical quantity of particles in this two-dimensional flow field and the physical quantity of particle transport in the z-direction can be written as the following equation:

$$Q_{pr}=-l'<C_t>\frac{db_{pr}}{dz} \qquad (2.25)$$

b_{pr} is the physical quantity moved by the particles, Q_{pr} is the average value of the physical quantity moved by the particles, and l' is the distance moved.

The particle kinetic stress (τ) is related to the amount of momentum change generated by the movement of each particle, and the average turbulent velocity $\langle C_t \rangle$ is used:

$$\tau_k=-\rho_s l'(C_t)\dot{\gamma} \qquad (2.26)$$

Transportation distance l' is the free movement distance of the particle before collision, and this time is t_f:

$$l'=<C_t>t_f \qquad (2.27)$$

Bringing the transportation distance l' into Eq. (2-44) and integrating $<C_t>$, the following equation is obtained:

$$\tau_k=\frac{\rho_s d_p}{3g_o}\sqrt{\frac{T}{\pi}}\,\pi \qquad (2.28)$$

20
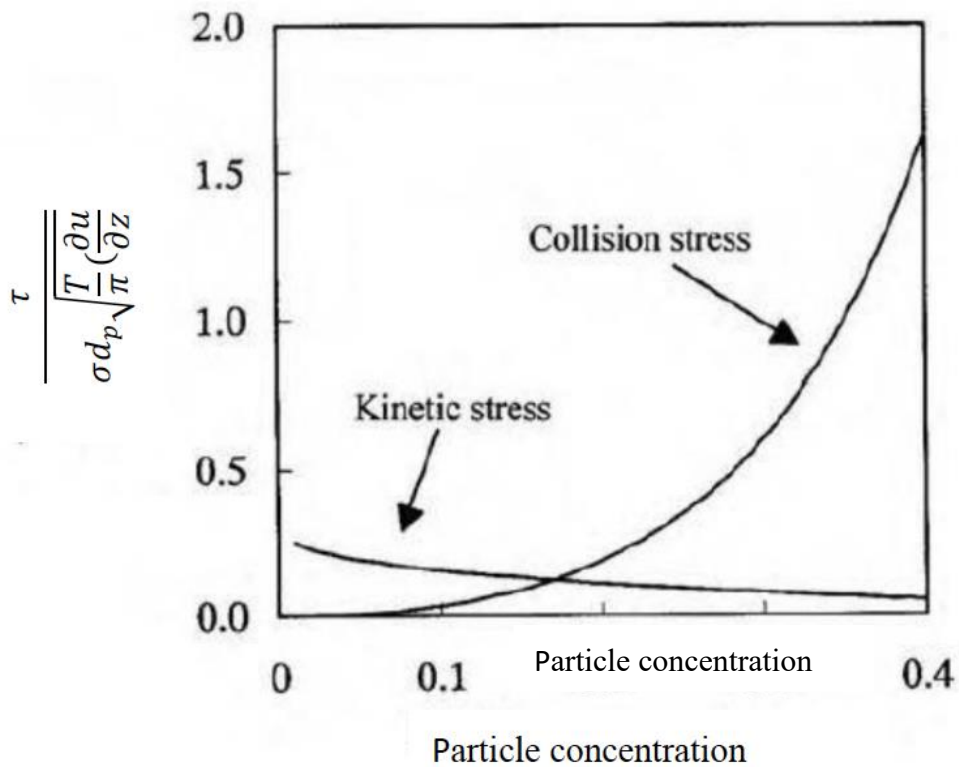
Figure 2.5 Size distribution of particle volume concentration in response to collision stress and particle kinetic stress, respectively (σ is ρ_s in the figure) [1]

Figure 2.5 shows that for a gravelly geotechnical flow with a sub-bed volume concentration of C_b=65% and a rebound coefficient of e=0.85, the collision shear stress τ_c starts to be larger than the particle kinetic stress τ_k if the particle volume concentration C_v is larger than 15%.

2.1.6 Generalized Viscoplastic Rheology Models

Chen (1988) believes that viscosity, plasticity, and collision in particulate fluids must be taken into account, so the above three roles are combined together and written as a general formula for the presentation of particulate flow, which is a generalized

21

viscoplastic fluid model or GVF model, and is also a type of the yield power law model, which is a type of the yield power law model with a yielding stress. It is also a kind of yield power law model. The mathematical equation is
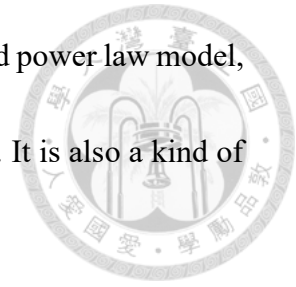
$$\tau = \tau_y + \mu_{gvn}\dot{\gamma}^\vartheta = c*\cos\varphi_c + p*\sin\varphi_c + \mu_{gvn}(\dot{\gamma})^\vartheta \qquad (2.29)$$

Where, and P are the fluid cohesion and flow pressure respectively, φ_c is the angle of internal friction of the particles, μ_{gvn} is the consistency index of this model, and ϑ is the index of flow characteristics. The authors concluded that this model contains both the Bingham and Bagnold expansion modes, and therefore both modes can be considered as submodels of the GVF model. However, this model has five unknowns and is not easy to use.

2.1.7 Quadratic Model

O'Brien et al. (1985) suggested that the Bingham model is more suitable for low shear strains.O'Brien et al. (1985) suggested that the Bingham model is more suitable for the case of low shear strain, where collision or turbulence of the particulate flow is not obvious, and therefore the rheological characteristics of the particulate flow can be described.

However, when the flow is a high concentration of particles, the shear strain rate is on the high side, and the flow is in the low side of the shear strain rate, so that the rheological characteristics of the particulate flow can be described.

22
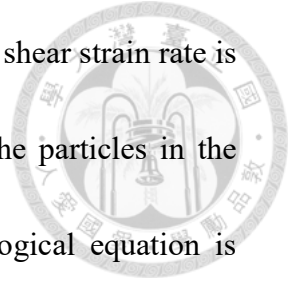
However, when the flow is a highly concentrated granular flow, the shear strain rate is high, or the concentration of fine-grained granular fluid is low, the particles in the granular fluid may be turbulent and collision, therefore, a rheological equation is proposed to consider the characteristics of viscous-plastic, turbulent and collision simultaneously.

Therefore, O'Brien proposed a rheological equation that considers viscoplasticity, turbulence and collision characteristics simultaneously, and this rheological model is also called the simulated plasticity model.Later in 1993, O'Brien et al. developed a finite-difference particle flow model based on the rheological model developed in 1985.In 1993, O'Brien et al. developed the finite-difference analysis software FLO-2D for particle flow based on the rheological model studied in 1985, and the rheological model is shown in the following equation:

$$\tau = \tau_{cy} + \tau_{mc} + \tau_v + \tau_c + \tau_t \tag{2.30}$$

τ_{cy}：Cohesive yield stress

τ_{mc}:Mohr-Coulomb shear stress

τ_v：Viscous shear stress

τ_t：Turbulent shear stress

τ_c：Crash Discrete Shear Stress

Then the physical meaning of (2.30) is defined (its will be the same as equation (2.1)):

23

$$\tau = \tau_{OB} + \mu_B(\dot\gamma) + (\alpha_i \rho_s \lambda^2 d_p{}^2 \ \rho_m l_m{}^2) \ \dot\gamma^2 \tag{2.31}$$

where $\tau_{OB} = \tau_{cy} + \tau_{mc}$, and usually the buckling stress τ_{OB} of the binomial flow is set

to the Bingham buckling stress τ_B. The definition of lm in Eq. (2.17), lm is the Prandtl

mixed doping length coefficient, as defined by Julien et al. (1991) $lm = 0.4$, as the depth

of granular flow mobility.

2.1.8. Voellmy Rheological Modeling

This rheological model combines Coulomb friction and turbulence. This rheology

is more commonly used when the particles fall off quickly and the volume

concentration of coarse particles (C_{vg}) is very large, and the rheological equation is as

follows [3]:

$$\tau_{vo} = \sigma_n f_v + \frac{\rho_d g U^2}{\rho_m l_m^2} \tag{2.32}$$

σ_n：Internal positive force on the shear surface due to mutual contact between

particles

f_v：Friction between particles

ρ_d: Overall particle flow density ($\rho_d = C_{vg} * \rho_s + (1 - C_{vg}) * \rho_m$)

g：Gravitational acceleration

ρ_m：Density of particles in the slurry fraction

l_m：Prandtl (Mixing length coefficient)

2.2 Particle Analysis

The motion of particles in a fluid is affected by fluid friction, Brownian motion, and electrostatic forces, as shown in the figure below. Friction is the dominant force and the particle trajectory is close to the streamline of the flow field. The Brownian force adds a small change in direction to the particles. If there is an electric charge on the surface of the tubing and on the particles, electrostatic bouncing and attraction occurs and changes the direction of the particles.
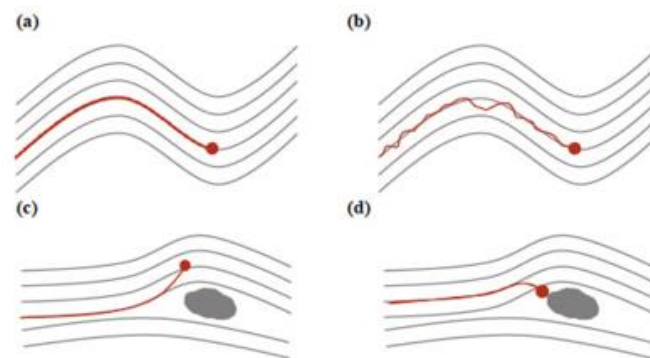
Figure 2.6 Particle movement influenced by (a) friction with fluids,(b) Brownian motion (c) electrostatic bouncing and (d) electrostatic attraction[4]

By combining all the factors, it is possible to predict the motion and final position of the particles in the fluid. The system can be solved by the following equations:

$$d\vec{v}=\gamma(\vec{u}(x)-\vec{v}(x))dt+\frac{Q\vec{E}(x)}{m}dt+\vec{B}(t)+\vec{f}dt \qquad (2.33)$$

$$\gamma = 6\pi\mu\frac{R}{C_cm} \qquad (2.34)$$

$$\vec{B}(t)=\sigma d\vec{w}(t) \qquad (2.35)$$

$$\sigma^2 = \frac{C_c k_B T}{m} \tag{2.36}$$

$$f = 0 \tag{2.37}$$

where $\gamma(\vec{u}(x) - \vec{v}(x))dt$ corresponds to the particle and the fluid, $\frac{Q\vec{E}(x)}{m}dt$ is the electrostatic force, B(t) is the diffusive (Brownian) motion, $\vec{f}dt$ is the user-defined external force, v is the particle velocity, u is the fluid velocity, γ is the friction coefficient, μ is the dynamic viscosity, R is the particle radius, C_c is the Cunningham correction, m is the particle mass, and dW is the temperature. C_c is the Cunningham correction, m is the particle mass, λ is the mean free path, Q is the particle charge, E is the electric field, kB is the Boltzmann constant, dW is the 3D Wiener measure, and T is the temperature.

To calculate the Cunningham corrections, it is necessary to know the mean free path λ. Jennings et al. found that the mean free range is equal to 6.635×10^{-8}m , similar to the default Cunning Lambda of 6.6×10^{-8}m

2.3 Stress Analysis

When simulating the flow of particles in the tubing, settling occurs and collisions occur with the tubing surface, resulting in energy loss in particle motion. The Hanmaker model measures the energy loss between particle collisions by comparing the adhesion and velocity of the particles. According to the "Lifshitz" theory, the van der Waals force between two surfaces of radius R is given by the following equation:

$$F = \frac{HR}{6d^2} \tag{2.38}$$

26
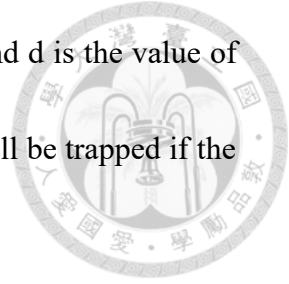
where F is the van der Waals force, H is the Hanmaker constant, and d is the value of

the cutoff separation distance. In the Hanmaker model, a particle will be trapped if the

following inequality occurs:

$$v^2 \leq \frac{HR}{6d^2} \tag{2.39}$$

Where V is the particle velocity, H is the Hanmaker constant, ao is the attachment

distance (equilibrium distance between particle and surface: 4 Å), and R is the particle

radius. The Hanmaker constant defines the ratio of energy not absorbed by the collision,

which means that if the constant is zero, the particle will be trapped, and if the constant

is equal to 1, it will be reflected with the same velocity.

Particle migration modes on surfaces have been studied by many researchers and can

be categorized into departure, adhesion and sliding modes under various conditions. A

brief description of the work of Hwang et al. which is applied to this study, is presented

below. Exit mode. In the following figure, the net external force acting on particle can

be divided into tangential part F_o, and normal part F_n,. If the direction of F° is the same

as the unit normal contact vector , the combined force acting on particle o is equal to

F_o , and the net torque wo be zero. According to Newton's second law of motion, the

particle o will leave its contact point and move linearly $a_O (= F_O/m_O)$ toward F_o in the

direction of the acceleration viscous and sliding modes. For the other two modes

particle migration, adhesion mode and sliding mode, if the direction of F_O. is opposite

27

to the unit normal contact vector e, then the normal force F, friction F_f for both modes

should be taken into account to calculate the net force and torque o acting on the particle

as shown in Figure 2.7 (b) and (c). In these cases, the particle o will move only by

rolling (adhesion mode) or by rolling and sliding (sliding mode) the surface of other

particles as follows:
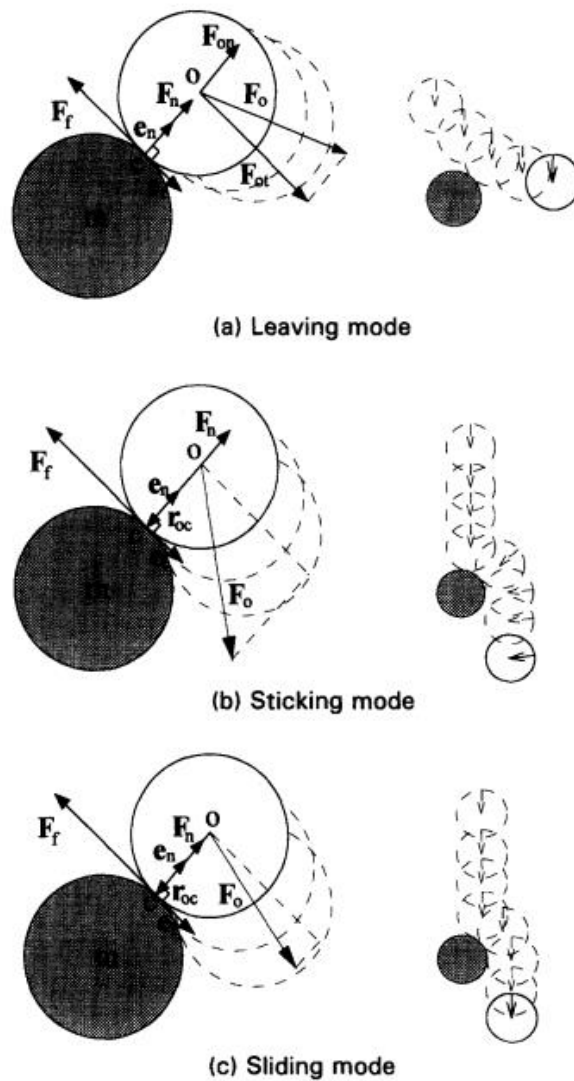
Figure 2.7 The net external force acting on particle [5]

2.4 Mechanical Properties of Particle Layers

The accumulation of a large number of particles will form a granular body, and the accumulation parameters of the granular body, such as void ratio, accumulation rate, coordination number, specific surface area, etc., have a significant effect on the mechanical properties and stability of the granular body [10]. The accumulation parameters of the hydrate deposition layer in the pipe wall mainly include void ratio, void distribution, accumulation rate, coordination number, specific surface area, etc. Among them, the accumulation parameters of the hydrate deposition layer in the pipe wall have a significant influence on the mechanical properties and stability of the particulate matter. Among them, the three parameters that have the greatest influence on the mechanical properties and stability of the hydrate sedimentary layer in the pipe wall are void ratio, accumulation rate and coordination number. The following is a brief introduction to these three parameters. (1) Void fraction ε The volume fraction of the void space between hydrate particles in the hydrate sedimentary layer can be calculated by equation (1).

$\varepsilon = \dfrac{V_v}{V_d} = \dfrac{V_d - V_h}{V_d}$ where(1) V_d, V_v, V_h are the volume of the hydrate sedimentary layer, the volume of the void in the sedimentary layer and the volume of hydrate in the

29

sedimentary layer. (2) accumulation rate λ tube wall hydrate sedimentary layer hydrate particles accounted for the volume fraction, calculated as shown in equation (2).$\lambda=\dfrac{V_v}{V_d}=1-\varepsilon$-(2) (3) Coordination number The number of contact points between each hydrate particle and other surrounding hydrate particles in the hydrate deposition layer of the NC pipe wall.
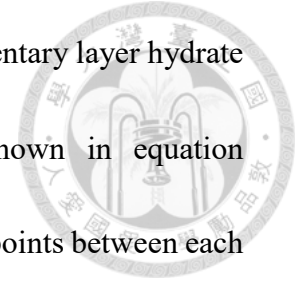
2.5 3D Printing

2.5.1 Advantages of 3D Printing

1) product complexity, diversity and cost is not relevant: traditional manufacturing, the more complex the shape of the product, the higher the cost of its production, at the same time, traditional manufacturing equipment less functional or single, can be processed in a limited number of product shapes, and a 3D printer, it can print a variety of shapes of products, whether complex or simple shapes of the object. It does not require mechanical processing or pre-production of any mold, which reduces the complexity of the product manufacturing difficulties, shorten the research and development cycle.

2) Zero-skill manufacturing: Traditional industries require several years of apprenticeship to master the required skills, mass production and computer-controlled manufacturing machines reduce the skill requirements, but traditional manufacturing machines still require skilled professionals to adjust and calibrate the machines. To

30

make the same complex product, an individual designs it in a computer, then translates the complex process into numbers and sends them to a 3D printer to be manufactured. Throughout the process, the user does not need to master a variety of complex manufacturing processes and processing skills, which significantly reduces the technological threshold of the manufacturing industry.
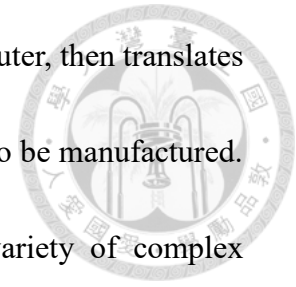
3)Advantages of customization: 3D printing can realize on-demand production, reducing the physical inventory of enterprises, avoiding the waste of resources in mass production of a large number of undelivered goods, more environmentally friendly, and even products can be printed on demand near the location, thereby reducing the logistics and transportation of products. The above advantages make 3D printing is very suitable for the following types of commodities rapid manufacturing (1) complex structures, such as traditional methods difficult to process the free-form surfaces, complex internal runners, and even can not be processed in the internal hollow structure (2) customized goods, such as jewelry, human organs, and other customized goods, small batch production and mass production of products before the research and development of the experimental production (3) high-value-added products, such as Aerospace, biomedical and other.

Domestic and foreign research and application, 3D printing technology and traditional mechanical processing, first of all, it is in the product dimensional accuracy

and surface quality and the latter difference is relatively large, the post-processing is more cumbersome, product performance is not up to the requirements of many metal structures: Secondly, it is in the processing speed, as well as the efficiency of large-scale production is still relatively low, can not fully satisfy the needs of the industrial sector, so 3D printing is a revolutionary breakthrough in the traditional manufacturing technology, though the Therefore, although 3D printing is a revolutionary breakthrough in traditional manufacturing technology, but it can not completely replace the cutting, casting and other traditional manufacturing technology, the two should be mutually supportive complementary, common improvement and development of a benign cooperative relationship.
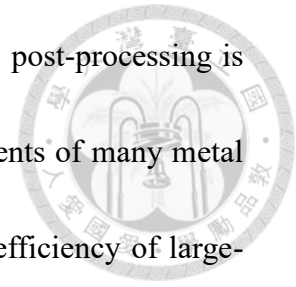
2.5.2 3D Printing Classification

The professional name of 3D printing is "Additive Manufacturing": Additive refers to the 3D printing through the deposition of raw materials or adhesive material layers have been structured into three-dimensional solid manufacturing method. Therefore, Huddy and Melba according to the material combination of 3D printing into two categories: (1) selective deposition: (2) selective adhesive method [1] then the use of material forms and process realization methods, will be subdivided into the following five categories: (1) powder or filament materials, high-energy beam sintering, melting molding, such as Selective Laser Sintering, Selective Laser Melting, Laser engineering

32

Net Shaping, LENS, etc. ((2) filament extrusion hot melt molding, such as FDM, etc.

(3) liquid resin light-curing molding, such as SLA, DLP, etc. (4) liquid spray molding,

three-dimensional spray printing, etc. (5) sheet / board / block material, such as the

annual connection or welding molding, such as layered solid manufacturing (LOM),

etc..
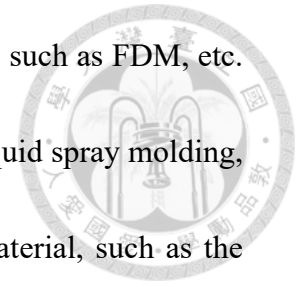
The following is a brief introduction to the representative technology methods as

follows:

1. Selective Laser Sintering

SLS is also known as selective laser sintering, the principle of the process is to lay a

layer of powder material (metal powder or non-metallic powder) in advance in the table,

the laser under the control of the computer, in accordance with the interface contour

information, the solid part of the powder for sintering, and then continue to cycle, layer

after layer of stacking molding.

The greatest advantage of the SLS process is the wide selection of materials, such

as ABS, metal and ceramic powders, which can be sintered. The sintered portion of the

powder becomes the support structure for the sintered portion, so there is no need to

consider a support system.

The disadvantages of SLS are: the prototype structure is loose and porous, and

there is internal stress, the production of variability; the generation of ceramic and metal

33

parts after treatment is more complex; the need for preheating and cooling; molding surface rough and porous, and subject to the powder particle size and laser spot limitations; molding process produces toxic gases and powders, polluting the environment.
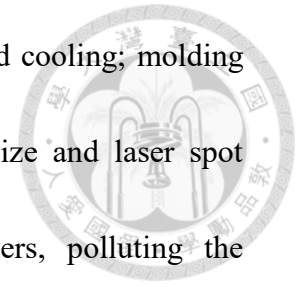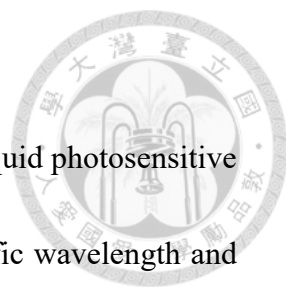
2. Fused Deposition Molding

FDM is a process in which a filamentary hot melt material is heated and melted while a three-dimensional nozzle, controlled by a computer, selectively applies the material to the table according to the cross-section profile information, and then rapidly cools it down to form a layer of the cross-section. After one layer is formed, the machine table is lowered by one height to form the next layer. The next layer is formed until the whole solid shape is formed. There are many types of molding materials, generally thermoplastic materials, such as ABS, PC, and filament material. The molded parts have high strength and high precision and are mainly suitable for small plastic parts.

Each layer of FDM process is stacked on top of the previous layer, which plays a positioning and supporting role for the current layer. When there is a big change in shape, the contour of the upper layer can not provide sufficient positioning and support for the current layer, which requires the design of some auxiliary structure "support" to provide positioning and support for the subsequent to ensure the smooth realization of the molding process.

34

3. Light-curing molding

SLA is the earliest practical rapid prototyping process, using liquid photosensitive resin as raw material, the principle of the process is to use a specific wavelength and intensity of the laser focused on the surface of the light-curing material, so that the point to line, from line to surface sequential solidification, to complete a layer of the drawing operation, and then lift the table in the vertical direction of the height of a layer, and then curing another layer. The layers are then stacked to form a three-dimensional entity. SLA process has the advantage of higher precision, good surface effect, so it is mainly used in the manufacture of a variety of molds, models, etc., parts production is completed after grinding, can be removed from the layers of the stacking marks, SLA molding of parts in general in the layer thickness of 0.1 to 0.15mm. Years of research to improve the cross-section scanning method and resin molding properties, so that the highest precision of the process has been able to reach 0.016mm.

The limitations of SLA are: the need for support, shrinkage of the resin leading to loss of accuracy, and the toxicity of the light-curing resin. In addition, light curing process running costs are very high, light curing equipment raw materials are very expensive, there are not many types of light curing equipment parts are manufactured, but also need to be cured in the UV curing box to ensure the strength of the parts.

4. 3D Printing
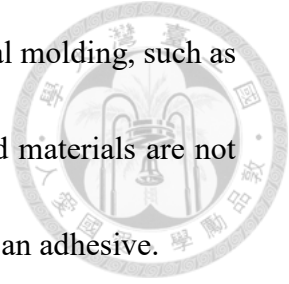
The process is similar to the SLS process, using powder material molding, such as ceramic powder, metal powder. The difference is that the powdered materials are not connected together by sintering, but passed through the nozzle with an adhesive. 3DP is a method of using micro-droplet spray technology, its specific process is as follows: the nozzle under computational control, in accordance with the current layered cross-section of the information, in advance of a layer of powder material, selective spray adhesive.

The powder, so that part of the powder to stick up, forming a thin layer of the cross-section, the last layer of molding is completed, the workbench to reduce the thickness of the layer, the next layer of powder, and then selective spraying of adhesive, molding film and has been shaped parts bonded together; and so on and so forth until the parts processing is completed. The area not bonded by the spray is dry powder, which plays a supporting role in the molding process and is easier to remove after the molding process is completed.

3DP technology has the advantage of fast forming speed, no support structure, and can output color printing products, the maximum output of 390,000 colors, color is very rich, but also in the appearance of the color, the print product is closest to the finished product of the 3D printing technology. 3DP technology has its shortcomings, first of all, the direct finished product of the strength of the powder bonding is not high, can only

36

be used as only as a test prototype, and secondly, due to powder bonding, the powder

bonding is not a good choice. Secondly, due to the working principle of powder bonding,

the surface of the finished product is not as bright as SLA, and the fineness is also at a

disadvantage. Therefore, a series of post-processing tools are generally required in

order to produce products with sufficient strength. In addition, the technology to

produce the powder for the material in question is more complex and costly.

5.Digital Light Processing Molding

DLP process is the use of light curing and projector DLP technology through the

visible light will be cured layer by layer of photosensitive resin into the 3D object, 3D

object from top to bottom layer by layer to create a stack.

It is very similar to the previous SLA light curing, the only difference is that the SLA

light is gathered into a point on the surface movement, while the DLP is the light on a

surface, a bit like a projector, layer by layer light curing, so the speed is faster than the

same type of SLA three-dimensional flatbed printing technology.

At the same time, it uses a high-resolution digital light processing projector to cure the

liquid photosensitive resin, which can realize ultra-thin 3D printing layer, high molding

accuracy, in material properties, details and surface finish are good. 5.Digital Light
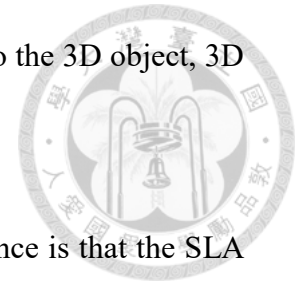
Processing Molding

DLP process is the use of light curing and projector DLP technology through the

visible light will be cured layer by layer of photosensitive resin into the 3D object, 3D object from top to bottom layer by layer to create a stack.

It is very similar to the previous SLA light curing, the only difference is that the SLA light is gathered into a point on the surface movement, while the DLP is the light on a surface, a bit like a projector, layer by layer light curing, so the speed is faster than the same type of SLA three-dimensional flatbed printing technology.

At the same time, it uses a high-resolution digital light processing projector to cure the liquid photosensitive resin, which can realize ultra-thin 3D printing layer, high molding accuracy, in material properties, details and surface finish are good.

5. Layered Solid Manufacturing (LOM)

The LOM process is based on the contour lines of each section of a 3D CAD model, which is controlled by a computer that sends commands to control the laser cutting system to move in the X and Y directions. The feeding mechanism feeds the tool (e.g., coated paper, plastic foil), which is coated with hot solvent on the floor, to the table in sections. The laser cutting system follows the contours of the cross-section segments extracted by the computer and uses a carbon dioxide laser beam to cut the paper on the table along the contour lines of the foil and to cut the uncontoured areas of the paper into small pieces.

LOM is suitable for the production of medium and large-sized components, small

deformation, shorter molding time, long life of the laser, the finished product has good mechanical properties, without the need to design and manufacture the supporting structure, suitable for product design concept modeling and functional test parts. Advantages: Faster molding speed. Since only the contour of the laser beam is used to cut, not scanning the entire cross-section, the molding speed is very fast, and thus it is often used for processing large parts with simple internal structures.
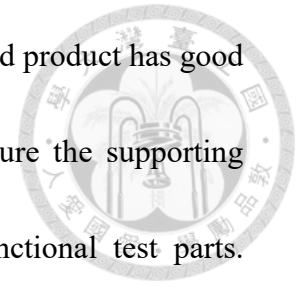
2.5.3 3D Printing Process

Broadly speaking, the complete process of 3D printing mainly includes five steps.

(1) 3D model generation: the use of three-dimensional computer-aided design (CAD) or modeling software modeling or through three-dimensional scanning equipment, such as laser scanner, structured light scanner to obtain the generation of 3D model data, the 3D model data format obtained at this time may vary due to different methods, some of which may be the scanning of the point cloud data obtained, and some of which may be the generation of NURBS surfaces modeled. Some may be point cloud data from scanning, while others may be NURBS surface information generated by modeling.

(2) Data format conversion converts the 3D model into an STL file for 3D printing. STL is the standard format used for 3D printing. It is a small triangle surface as the basic units

(3) slicing calculation: computer-aided design technology (CAD) on the triangular

mesh format of the 3D model for digital slicing, it will be cut into a piece of thin layers, each layer corresponds to the future 3D printing of the physical layer.
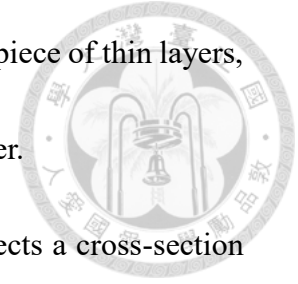
(4) print path rules: each virtual thin layer obtained by slicing reflects a cross-section of the final printed object, in the future 3D printing printer needs to carry out a lenticular scanning to fill the inner contour, therefore, the need to plan a specific print path and optimization, in order to get a faster and better slicing.

(5) 3D printing: 3D printer according to the above slicing and slicing path information to control the printing process, print out each layer will be stacked layer by layer, until the final printing object molding.

Chapter 3 METHODS & THEORIES

3.1 Governing Equations

The governing equation for the liquid phase in a two-phase flow system is as follows(Drew and Passman,1998)

$$\frac{\partial \phi_c}{\partial t} + \nabla \cdot (u_c \phi_c) = 0 \tag{3.1}$$

$$\frac{\partial \phi_c \rho_c u_c}{\partial t} + \nabla \cdot (u_c \phi_c) = -\phi_c \rho_c \nabla p + \phi_c(\rho_c \nu \nabla^2 u_c) + \phi_s \rho_p M_{cd} \tag{3.2}$$

ϕ_c is the volume fraction of the liquid phase, u_c is fluid velocity, ϕ_s is volume fraction of a single particle, ρ_c is liquid phase density, P is dynamic pressure,already divided byρ_c, ν is fluid kinematic viscosity coefficient, M_{cd} is momentum exchange between phase states.And continuity equation and motion equation of particle phase(Maxey and Riley,1983)

As follows

$$\frac{\partial \phi_s}{\partial t} + \nabla \cdot (u_p \phi_s) = 0 \tag{3.3}$$

$$m_p \frac{du_p}{dt} = 3\pi d_p \mu(u_{c|p-u_p}) - m_c \nabla_p + C_{vm} m_c(\frac{Du_c}{Dt}|_p - \frac{dup}{dt}) + (m_p - m_c)g. \tag{3.4}$$

u_p is particle velocity,m_p is single particle mass, $m_c = \rho_c \pi d_p^3/6$ is fluid mass, $u_{c|p}$ is the velocity of the fluid at the location of the particle,$D/Dt = \partial/\partial t + u_c \cdot \nabla$ is substantial derivative for fliud.And the first item on the right side of the equal sign in formula (3.4) is Stokes' drag, second item is dynamic pressure gradient of background flow field,third

41
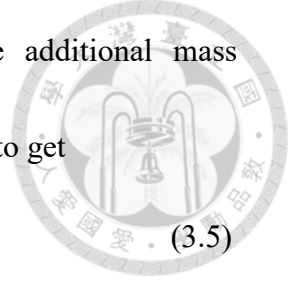
item is additional mass(Auton et al.,1988), where C_{vm} is the additional mass

factor,fourth item is gravity and buoyancy. Then divide (3.4) by m_p to get

$$\frac{du_p}{dt}=\frac{18\mu(u_{c|p}-u_p)}{\rho_p d_p^2}+(1-\frac{1}{s})g-\frac{1}{s}\nabla p+\frac{C_{vm}}{s}(\frac{Du_c}{Dt}\Big|_p-\frac{du_p}{dt}) \tag{3.5}$$

Where $s=\rho_p/\rho_c$, thus the formula above can be simplified as below

$$\frac{18\mu(u_{c|p}-u_p)}{\rho_p d_p^2}=\frac{u_{c|p}-u_p}{\tau p} \tag{3.6}$$

Disassemble the additional mass on the right side of the equal sign in Equation 3.5 and

transpose it to get

$$(1+\frac{C_{vm}}{s})\frac{dup}{dt}=\frac{u_{c|p}-u_p}{\tau p}+(1-\frac{1}{s})g-\frac{1}{s}\nabla p+\frac{C_{vm}}{s}\frac{Du_c}{Dt}\Big|_p \tag{3.7}$$

And by the formula (2.5),we can simplify momentum exchange expression as below

$$M_{cd}=-\sum_{i=1}^{Np}[\frac{u_{c|p.i}-u_{p,i}}{\tau p}+\frac{C_{vm}}{s}(\frac{Du_c}{Dt}]\Big|_p-\frac{du_{p,i}}{dt})] \tag{3.8}$$

Where the first item on the right side of the equal sign in formula (3.8) is Stokes'

drag,second item is additional mass.And $\sum_{i=1}^{Np}\frac{du_{p,i}}{dt}$ represent the sum of the forces

imparted to the fluid by particles in the control volume.Bring formula (3.8) to formula

(3.2) and divide by ρ_c to get

$$-C_{vm}\phi_s\sum_{i=1}^{Np}\frac{du_{p,i}}{dt}+\frac{\partial\phi_c u_c}{\partial t}+\nabla\cdot(u_c\phi_c)+\nabla\cdot(u_c\phi_c u_c)$$

$$=-\phi_c\nabla p+\phi_c(\nu\nabla^2 u_c)-s\phi_s\sum_{i=1}^{Np}[\frac{u_{c|p.i}-u_{p,i}}{\tau p}+\frac{C_{vm}}{s}(\frac{Du_c}{Dt}\Big|_p] \tag{3.9}$$

Equations 3.7 and 3.9 can be rewritten as a coupled two-phase flow system.

$$\begin{bmatrix} 1+\frac{C_{vm}}{s} & 0 & \\ 0 & \ddots & \\ -C_{vm}\phi_s & \dots & 1 \end{bmatrix}\begin{bmatrix} \frac{du_{p,1}}{dt} \\ \vdots \\ \frac{\partial u_c}{\partial t}+\nabla\cdot(u_c\phi_c u_c) \end{bmatrix}$$
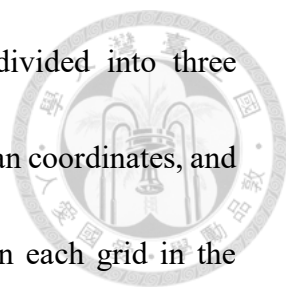
42

$$
=\begin{bmatrix} \frac{u_{c|p,1}-u_p}{\tau_p} \\ \vdots \\ -s\phi_s\sum\frac{u_{c|p}-u_p}{\tau_p} \end{bmatrix}+\begin{bmatrix} -\frac{1}{s}\nabla p \\ \vdots \\ -\phi_c\nabla p \end{bmatrix}+\begin{bmatrix} \left(1-\frac{1}{s}\right)g \\ \vdots \\ \phi_c\nu\nabla^2 u_c \end{bmatrix}+\begin{bmatrix} \frac{C_{vm}}{s}\frac{Du_c}{Dt}|_{p,1} \\ \vdots \\ -\sum C_{vm}\phi_s\frac{Du_c}{Dt}|_p \end{bmatrix} \tag{3.10}
$$

and Equation 2.10 can be rewritten as below

$$
\begin{bmatrix} \frac{du_{p,1}}{dt} \\ \vdots \\ \frac{\partial u_c}{\partial t}+\nabla\cdot(u_c\phi_c u_c) \end{bmatrix} = A\begin{bmatrix} \frac{u_{c|p}-u_p}{\tau_p} \\ \vdots \\ -s\phi_s\sum\frac{u_{c|p}-u_p}{\tau_p} \end{bmatrix}+A\begin{bmatrix} -\frac{1}{s}\nabla p \\ \vdots \\ -\phi_c\nabla p \end{bmatrix}+A\begin{bmatrix} \left(1-\frac{1}{s}\right)g \\ \vdots \\ \phi_c\nu\nabla^2 u_c \end{bmatrix}
$$

$$
+A\begin{bmatrix} \frac{C_{vm}}{s}\frac{Du_c}{Dt}|_{p,1} \\ \vdots \\ -\sum C_{vm}\phi_s\frac{Du_c}{Dt}|_p \end{bmatrix} \tag{3.11}
$$

where matrix A as below

$$
A=\begin{bmatrix} 1+\frac{C_{vm}}{s} & 0 & 0 \\ 0 & \ddots & \\ -C_{vm}\phi_s & \cdots & 1 \end{bmatrix}^{-1}=\begin{bmatrix} \frac{1}{1+\frac{C_{vm}}{s}} & 0 & 0 \\ 0 & \ddots & \\ \frac{-C_{vm}\phi_s}{1+\frac{C_{vm}}{s}} & \cdots & 1 \end{bmatrix} \tag{3.12}
$$

The meaning of the matrix A is to divide the influence of the additional mass into the

contribution of each force

Particles in motion in fluid, We have not yet taken into account factors such as particle

rotation、Basset history force、Saffman lift and collide with each other, Now we

prototyping the model first, ignoring above. Substituing the equation(3.12)into(3.11) to

expand, we can get

$$
\frac{du_p}{dt}=\left(\frac{1}{1+\frac{C_{vm}}{s}}\right)\left[\frac{u_{c|p}-u_p}{\tau_p}+\left(1-\frac{1}{s}\right)g-\frac{1}{s}\nabla p+\frac{C_{vm}}{s}\frac{Du_c}{Dt}|_p\right] \tag{3.13}
$$

$$
\frac{\partial\phi_c u_c}{\partial t}+\nabla\cdot(u_c\phi_c u_c)=\phi_c(\nu\nabla^2 u_c)+\left(\frac{C_{vm}\phi_s}{1+\frac{C_{vm}}{s}}-s\phi_s\right)\sum\frac{u_{c|p}-u_p}{\tau_p}+\frac{C_{vm}\phi_d}{1+\frac{C_{vm}}{s}}\left(1-\frac{1}{s}\right)g
$$

$$+(\frac{C_{vm}\phi_s}{1+\frac{C_{vm}}{s}} - C_{vm}\phi_s) \sum \frac{Du_c}{Dt}|_p - (\phi_c + \frac{C_{vm}\phi_d}{1+\frac{C_{vm}}{s}})\nabla p. \qquad (3.14)$$

Equations (3.13) and (3.14) [11] are the momentum equations used in the solid-liquid system model in this study. In the momentum exchange term between phase states.

In addition to the Stokes drag force that has been considered in previous related studies, then we have added the effect of additional mass and operate through the inverse matrix. From equation(3.13), it can be found that the additional mass effect of the fluid on the particles decreases as the density ratio increases, In a solid-gas two-phase flow problem ,the density ratio of the solid-gas two-phase state is usually about O(1000), so the additional mass force on the solid state is ignored is a reasonable assumption, but the solid-liquid two-phase is not applicable. On the other hand, equation (2.14) shows that the additional mass force on the liquid phase is closely related to the volume fraction of the solid phase, that is, as the number of particles increases, the additional mass force on the liquid phase from the solid phase increases as well.

3.2 Particle Transport System

In this study, the Lagrangian description method is used to analyze the motion of the particles, i.e., the particles are considered as discrete individuals and the motion of the particles is pursued one by one, so that the correct transmission of particles between grids is one of the main points of this numerical model.

44

According to the independence of the movement, we will be divided into three orthogonal directions of the movement of the particles in the Cartesian coordinates, and the order of movement in different directions does not affect, then each grid in the transmission, only need to consider the information of the front and back of each grid, the calculation method as the Eulerian method of Advection scheme, compared to a direct move to the positioning of the method is relatively much simpler. Another consideration is that the flux of particles on the control surface is required in the subsequent part of the calculation, and it is easier to calculate the number of particles passing on the control surface by moving in three directions to obtain the flux of particles.

The essence of particle transfer is actually the exchange of information between grids, if a particle will leave the grid where it is currently located, then the information of the particle must be transferred to the grid where the particle stays in the next instant, conversely, if the particle will remain in the current grid after moving, then the information of the particle must be retained, when all the particles have finished moving in one direction, then all the grids must sort out the retained and received particle After all the particles have finished moving in one direction, all the grids must sort out the retained and received particle information before moving in the next direction, and the calculation method of the whole system can be described by Figure 3.1
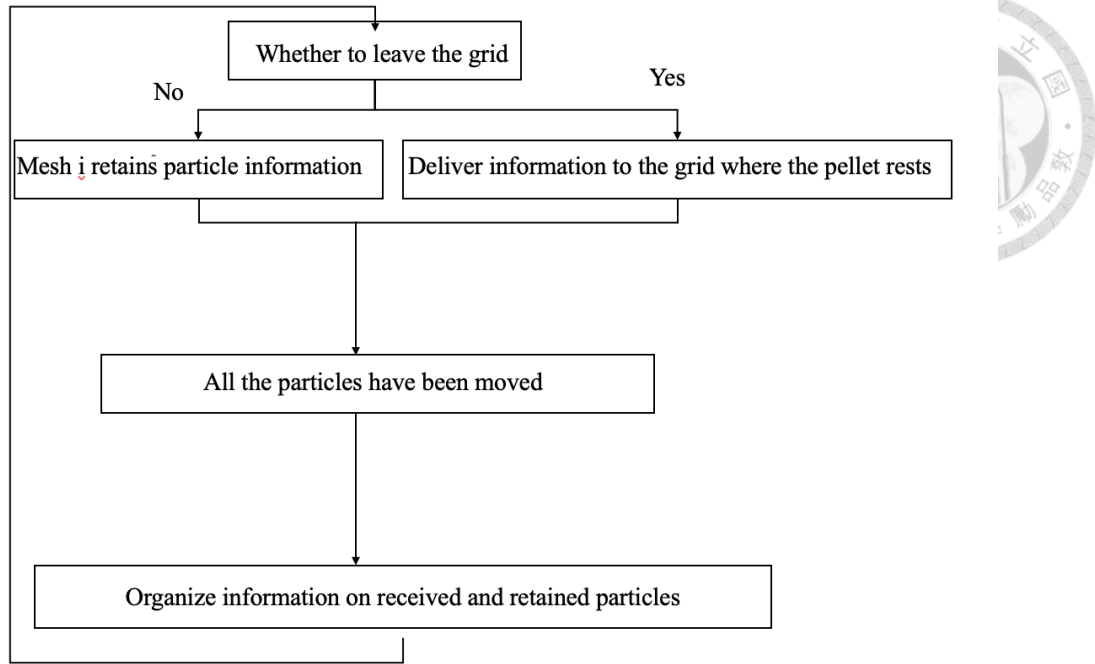
Figure 3.1 Particle Tracking Flowchart

The information about the particles includes the velocity position and displacement.

And the update of the particle position can be determined by the equation (3.15)

$$X_p^{n+1} = X_p^n + u_p^{n+1}\Delta t \tag{3.15}$$

We use u_p^{n+1} to determine whether the particles will leave the current grid, Since the

displacement of the pellet is calculated before the start of transmission, so in the process

of particle transmission, it is necessary to move the displacement information along

with the particles, so that it can be used in the other direction of transmission.

The boundary of the particle adopts inelastic collision, because no relevant

experimental data were found , so we first assume that the recovery coefficient of the

particle is 0.25. Because the velocity of the particle will change after colliding with the

wall, so the update method of the particle position must be slightly modified

46
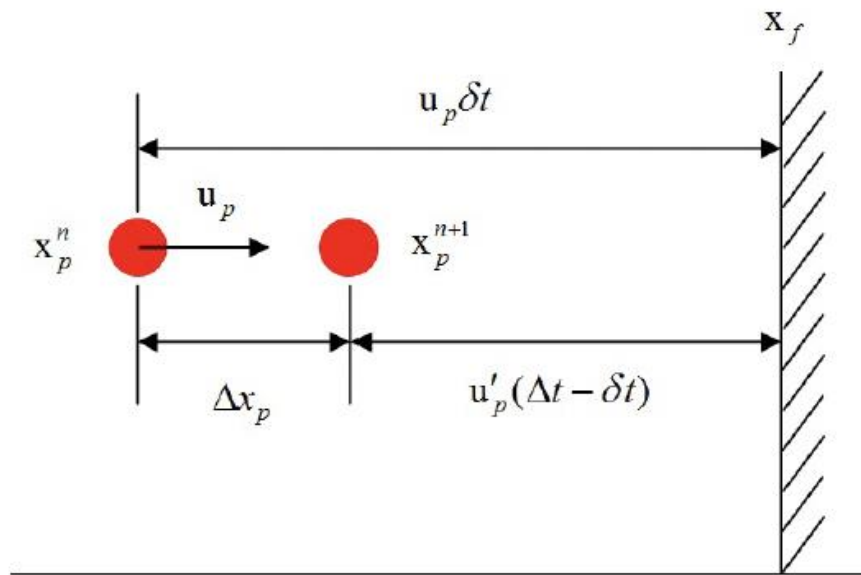
Figure 3.2 Wall collision schematic [7]

As shown in Figure 3.2, the horizontal direction is used as an example here, X_f is the wall position, X_p^{n+1} is the particle position before the collision, u_p is the horizontal velocity before the collision, u_p' is the horizontal velocity after the collision, Δt is the time interval for each step of the calculation, δt is the time required for the particle to reach the wall, ΔX_p is the displacement of the particle, and δt can be found by (2.16) equation

$$\delta t = \frac{X_f - X_p^n}{u_p} \tag{3.16}$$

And $u_p' = 0.25 u_p$, so the particle bounces back after moving the displacement as below

$$u_p'(\Delta t - \delta t) = 0.25 u_p(\Delta t - \delta t) \tag{3.17}$$

then Xp can be obtained

$$\Delta X_p = (X_f - X_p^n) + [\, u_p'(\Delta t - \delta t)\,] \circ \tag{3.18}$$

47

After obtaining ΔX_p, the position of the particle after rebounding X_p^{n+1} is

$$X_p^{n+1} = X_p^n + \Delta X_p \tag{3.19}$$

3.3 Numerical Method

3.3.1 Direct Numerical Simulation

The core algorithm is called the mapping method, which was proposed by

Chorin.A.J. in 1967, assuming that the flow is incompressible, and the governing

equation is of the following form

$$\nabla \cdot u_c = 0 \tag{3.20}$$

$$\frac{\partial u_c}{\partial t} + u_c \cdot \nabla u_c = \frac{1}{\rho_c}\nabla p + \nu\nabla^2 u_c + \nu\nabla^2 u_c \tag{3.21}$$
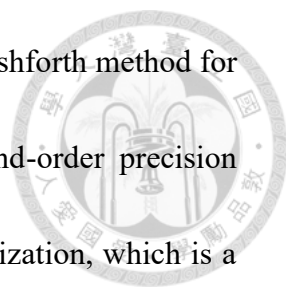
In equation (2.21), the gravity term has been balanced with the hydrostatic pressure,

and after decomposing it by the step-by-step method, we get

$$\frac{u_c^* - u_c^n}{\Delta t} = -u_c^n \cdot \nabla u_c^n + \nu\nabla^2 u_c^n \tag{3.23}$$

$$\frac{u_c^* - u_c^n}{\Delta t} = -\frac{1}{\rho_c}\nabla p^{n+1} \tag{3.24}$$

where u_c^n stands for the current speed, u_c^{n+1} for the next speed and u_c^* for the

intermediate speed, which is the transition product of the calculation process.

48

In the numerical model used in this study, we use the Adam-Bashforth method for the time discretization of the convective term, which is a second-order precision discretization method, and the Quick method for the spatial discretization, which is a third-order precision discretization method. As shown in Figure 3.3, the solid line is the center of the grid, i.e., the location of the pure quantity and vector definition, and the dashed line is the face of the grid. Assuming that $\emptyset$ is any pure or physical quantity, if u_c is in the +x direction, $\emptyset_e$ then can be obtained by interpolating $\emptyset_i$, $\emptyset_{i-1}$ and $\emptyset_{i+1}$. Conversely, if u_e is in the -x direction, then $\emptyset_e$ is obtained by interpolating $\emptyset_i$, $\emptyset_{i+1}$ and $\emptyset_{i+2}$, which is the principle of Quick discrete method.

The second term is the diffusion term. In the numerical model, we can describe the diffusion term by a matrix of $Nx \times Ny \times Nz$ by the second order central difference method, where Nx, Ny, Nz are the number of grids in three directions. The numerical model used in this study decomposes the matrix into diagonal and non-diagonal matrices, where the Crank-Nicolson method is used for the time discretization of the diagonal matrix and the Adam-Bashforth method is used for the time discretization of the non-diagonal matrix.

49
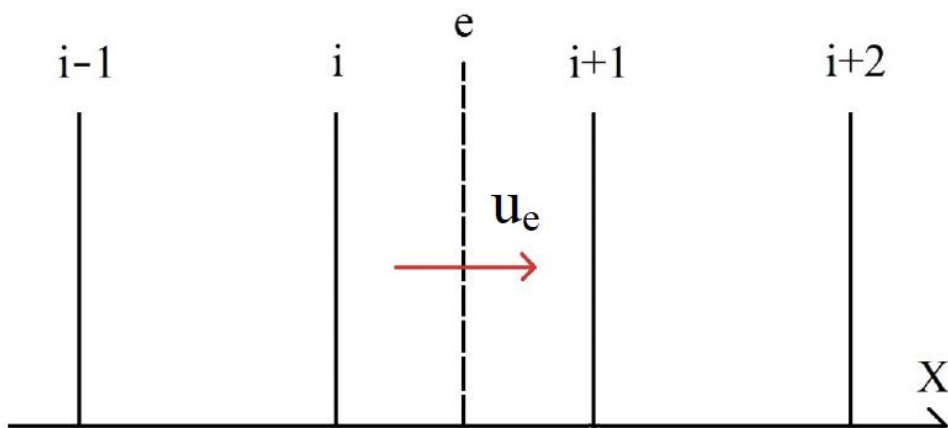
Figure 3.3 One-dimensional grid schematic diagram [7]

After solving u_c^* from equation 3.22 and taking the scatter of equation 3.23, we get

$$\nabla \cdot u_c^{n+1} - \nabla u_c^* = -\frac{\Delta t}{\rho_c} \nabla^2 p^{n+1} \tag{3.24}$$

and since $\nabla \cdot u_c^*$ satisfies equation (2.20), we have

$$\nabla \cdot u_c^* = \frac{\Delta t}{\rho_c} \nabla^2 p^{n+1} \tag{3.25}$$

And the poisson equation of Eq. (3.24) yields p^{n+1}, and u_c^* and p^{n+1} are substituted into

Eq. 3.23 to find u_c^{n+1}

The mapping method consists of three main steps, the process of finding u_c^* from

equation (2.22) is called the prediction step, solving the poisson equation is the pressure

step, and finally substituting u_c^* and p^{n+1} into equation (2.23) to find u_c^{n+1} is the

correction step. The fluid evolution method used in this study is a little different from

the original mapping method, but the computational principles are still the same.

$$\frac{\emptyset_c^n u_c^* - \emptyset_c^n u_c^n}{\Delta t} = \frac{3}{2}(C^n + D_E^n) - \frac{1}{2}(C^{n-1} + D_E^{n-1}) + \frac{1}{2}(D_I^{n+1} + D_I^n) + \frac{C_{vm}\emptyset_d^n}{1 + \frac{C_{vm}}{s}}(1 - \frac{1}{s})g$$

50

$$+(\frac{C_{vm}\varnothing_s}{1+\frac{C_{vm}}{s}}-s\varnothing_s)\sum_{i=1}^{Np}\frac{u_{c|p.i}-u_{p,i}}{\tau p}+(\frac{C_{vm}\varnothing_s}{1+\frac{C_{vm}}{s}}\frac{C_{vm}}{s}-C_{vm}\varnothing_s)\sum_{i=1}^{N_p}\frac{Du_c^{n-\frac{1}{2}}}{Dt}|p. \qquad (3.26)$$

$$\frac{\varnothing_c^{n+1}u_c^{n+1}-\varnothing_c^n u_c^*}{\Delta t}=-(\varnothing_c^n+\frac{C_{vm}\varnothing_d^n}{1+\frac{C_{vm}}{s}})\nabla p^{n+1} \qquad (3.27)$$

where C is the convective term, D_E is the non-diagonal matrix part of the diffusive term, D_I is the diagonal matrix part of the diffusive term, and $\varnothing_d$ is the volume fraction of all particles in the grid. For the momentum exchange between the phases, we use the first-order display method for time discretization, the program part of the approach is to add up the force given by all the particles in the current grid, and then process it together with the convection and diffusion items, and solve equation 3.26 to obtain u_c^*.

The solution of the pressure field differs greatly from the original mapping method, and must be coupled with the solid state and then analyzed, after introducing the calculation of the equation of motion of the particles will be explained together after the introduction of the method of calculating the equation of motion of particles

Since we want to have the most complete flow field in the process of verifying the numerical model, we adopt the numerical direct solution method to be responsible for analyzing the flow field. The source code of the numerical direct solution used in this study was developed by Zang et al (1994), which can handle complex boundaries from a curved fine grid and supports parallel calculations (Cui and Street 2001).

3.3.2 Particle Equation

After the complete numerical direct solution in Section 3.3.1, this section introduces the numerical method of the particle motion equation. As in equation (3.13), the particle equation of motion is discretized and decomposed in a stepwise manner to obtain

$$\frac{u_p^* - u_p^n}{\Delta t} = \frac{1}{1+\frac{C_{vm}}{s}} \frac{u_{c|p}^n - u_p^n}{\tau p} + \frac{1}{1+\frac{C_{vm}}{s}}(1-\frac{1}{s})g + \frac{1}{1+\frac{C_{vm}}{s}} \frac{C_{vm}}{s} \frac{Du_c^{n-\frac{1}{2}}}{Dt}|_p. \tag{3.28}$$

$$\frac{u_p^{n+1} - u_p^*}{\Delta t} = -\frac{1}{1+\frac{C_{vm}}{s}} \frac{1}{s} \nabla p^{n+1} \tag{3.29}$$

Where $u_{c|p}$ is the fluid velocity at the location of the particle, (2.28) is the prediction step of the particle phase.

In equation (3.28), except $\frac{Du_c}{D_t}|_p$, the rest of the physical quantities can be directly or by interpolation to find, and if you want to get $\frac{Du_c}{D_t}|_p$, you must first find the relationship with the inertia term of equation (3.2). Divide the inertia term of equation 3.2 by ρ_c to get

$$\frac{\partial \phi_c u_c}{\partial t} + \nabla \cdot (u_c \phi_c u_{cx}) \tag{3.30}$$

Expanding equation 3.30, we get

$$u_{cx} \frac{\partial \phi_c}{\partial t} + \phi_c \frac{\partial u_{cx}}{\partial t} + \phi_c u_{cx}(\nabla \cdot u_c) + u_c(\nabla \phi_c u_{cx}). \tag{3.31}$$

Equation 2.31 can be further expanded to give

$$u_{cx} \frac{\partial \phi_c}{\partial t} + \phi_c \frac{\partial u_{cx}}{\partial t} + \phi_c u_{cx}(\nabla \cdot u_c) + u_c(u_{cx}\nabla \phi_c) + u_c(\phi_c \nabla \cdot u_{cx}) \tag{3.32}$$

52

(3.32) After finishing the formula as

$$u_{cx}[\frac{\partial \phi_c}{\partial t} + \phi_c(\nabla \cdot u_c) + u_c \nabla \cdot \phi_c] + \phi_c[\frac{\partial u_c}{\partial t} + u_c \cdot \nabla u_{cx}] \tag{3.33}$$

The first term of equation 2.33 satisfies equation 2.1, so we can get

$$u_{cx}[\frac{\partial \phi_c}{\partial t} + \phi_c(\nabla \cdot u_c) + u_c \nabla \cdot \phi_c] + \phi_c[\frac{\partial u_c}{\partial t} + u_c \cdot \nabla u_{cx}] = \phi_c \frac{Du_{cx}}{Dt} \tag{3.34}$$

After discretizing equation 3.34 as

$$\frac{Du_c^{n-\frac{1}{2}}}{Dt} = \frac{1}{\phi_c^n}[\frac{\phi_c^n u_{cx}^n - \phi_c^{n-1} u_{cx}^{n-1}}{\Delta t} + \frac{3}{2}C^n - \frac{1}{2}C^{n-1}] \tag{3.35}$$

In (3.28), $u_{c|p}$ of Stokes resistance and $\frac{Du_c}{Dt}_{|p}$ of additional masses are difficult to

calculate directly on the position of the particles, and if the number of particles is large,

direct calculation is not an efficient method, so the mass point grid method must be

used to assist, and will be further explained in (3.3.3)

3.3.3 Quality Point Grid Method

The spirit of this method is to combine the Eulerian and Lagrangian descriptions

in our solid-liquid system model, which is to resolve the discrete particles in the

Eulerian mesh.

The Stokes resistance, dynamic pressure gradient and additional mass in the

equation of particle motion are physical quantities that are difficult to resolve directly

in the particle position, so the spirit of the mass point grid method must be used to first
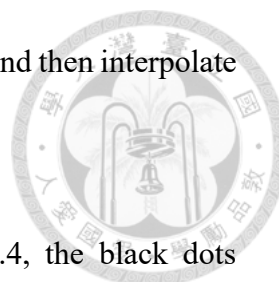
calculate the physical quantities mentioned above on the Euler grid, and then interpolate

the value of the particle position by trilinear interpolation.

In this two-dimensional case to illustrate, as shown in Figure 3.4, the black dots

represent the position of the pure quantities and vectors on the Eulerian grid, and the

red dots represent the location of any particle. The red dot represents the location of any

particle. If φ represents any pure quantity or vector, by linear interpolation, then φ is

$$\varphi_p = [\varphi_1 \frac{f_x}{\Delta x} + \varphi_2 (1 - \frac{f_x}{\Delta x})] \frac{f_y}{\Delta y} + [\varphi_3 \frac{f_x}{\Delta x} + \varphi_4 (1 - \frac{f_x}{\Delta x})](1 - \frac{f_y}{\Delta y}) \qquad (3.36)$$
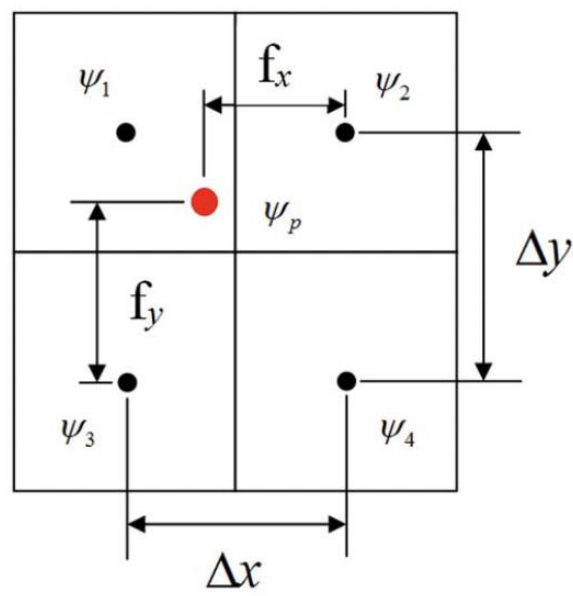
Figure 3.4 two-dimensional case [7]

3.3.4 Pressure Coupling

This part of this study and the traditional solid-liquid two-phase flow research is

the biggest difference, the early solid-liquid system model is the liquid phase and solid

54

phase are treated separately, the assumption that the particles do not occupy the volume, that is, "point particles", the analysis of the flow field only consider the liquid phase, that is, the general pure fluid flow field, after the post-processing part of the analysis of the behavior of the particles in the flow field, and do not consider the force of the particles to the flow field, that is, the so-called unidirectional coupling.

In this study, we inherited the theoretical framework of Chou et al (2014) and considered the momentum exchange between phases, i.e., two-way coupling, in addition to introducing the volume fraction in the governing equation of the liquid phase. We believe that the effect of particle volume is not only mentioned above, the mapping method should find the volume flux flowing on the control surface when analyzing the pressure of the flow field, and use it as the source term of the poisson equation. The traditional research method is to consider only the volume flux of the fluid, that is, the incompressibility of the fluid, but the control surface is not only the flow, but also the particles scattered in the flow field, so we believe that we should not only consider the volume flux of the fluid, but also the volume flux of the mixed fluid, and coupling the pressure equation of the two phases, that is, the aforementioned pressure coupling. As mentioned as belows the continuous equation of solid-liquid two-phase flow is

$$\frac{\partial \phi_c}{\partial t} + \nabla \cdot (u_c \phi_c) = 0 \tag{3.37}$$

$$\frac{\partial \phi_s}{\partial t} + \nabla \cdot (u_p \phi_s) = 0 \tag{3.38}$$
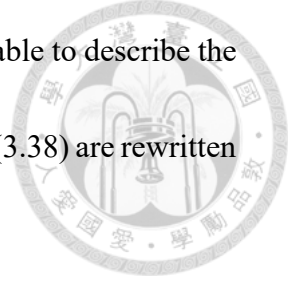
We believe that the particles are discrete individuals, so it is not suitable to describe the continuous equation in differential form, so the equations (3.37) and (3.38) are rewritten into integral form in the following form

$$\frac{\partial}{\partial t} \int \phi_c dV + \oint \phi_c (u_c \cdot n) dA = 0 \tag{3.39}$$

$$\sum_{i=1}^{N_p} \left(\frac{\partial}{\partial t} \int \phi_s dV + \oint \phi_s (u_p \cdot n) dA = 0 \right) \tag{3.40}$$

After discretizing equations 2.37 and 2.38, we get

$$\frac{\phi_c^{n+1} - \phi_c^n}{\Delta t} V + \int_{j=1}^{N} \phi_{c_j}^{\,n} u_{c_j}^{\,n} A_j = 0 \tag{3.41}$$

$$\frac{N_p^{n+1} \phi_s^{n+1} - N_p^n \phi_s^n}{\Delta t} V + \sum_{j=1}^{N} \sum_{i=1}^{N_s} \phi_{p_i}^{\,n} u_{p_i}^{\,n} A_j = 0 \tag{3.42}$$

$\phi_{c_j}^n$ is the area fraction of the fluid on the control surface, $u_{c_j}^n$ is the velocity of the fluid flowing over the control surface, A_j is the area of the control surface, N_p is the number of particles in the control volume, N_s is the number of particles passing through the control surface, and ϕ_{pi} is the area fraction of a single particle on the control surface.

Since $\phi_c + N_p \phi_s = 1$, the sum of equations (3.41) and (3.42) yields

$$\sum_{j=1}^{N} \phi_{c_i}^{\,n} u_{c_i}^{\,n} A_j + \sum_{j=1}^{N} \sum_{i=1}^{N_s} \phi_{p_i}^{\,n} u_{p_i}^{\,n} A_j = 0 \tag{3.43}$$

We refer to equation (3.43) as the incompressibility of the mixed fluid Following 3.3.1 and 3.3.2, after finding u_c^* and u_p^* from the prediction step, this section further explains how to solve for the pressure field. The pressure equation for the solid-liquid system is as follows

$$\frac{\phi_c^{n+1} u_c^{n+1} - \phi_c^n u_c^*}{\Delta t} = -\left(\emptyset_c^n + \frac{C_{vm} \emptyset_d^n}{1 + \frac{C_{vm}}{s}} \right) \nabla p^{n+1} \tag{3.44}$$

56

$$\frac{u_p^{n+1} - u_p^*}{\Delta t} = -\frac{1}{s+C_{vm}} \nabla p^{n+1} \qquad (3.45)$$

Multiplying equation 3.31 by ϕs and taking the dispersion together with equation 3.29

and substituting it into Gaussian dispersion theorem gives

$$\frac{1}{V}\sum_{j=1}^{N} \phi_{c_i}^{n} u_{c_i}^{n} A_j - \frac{1}{V}\sum_{j=1}^{N} \phi_{c_i}^{*} u_{c_i}^{*} A_j = \frac{\Delta t}{V}\sum_{j=1}^{N}\left(\phi_{c_i}^{*} + \frac{C_{vm}}{1+\frac{C_{vm}}{s}}\sum_{i=1}^{Ns}\phi_{p_i}^{*}\right)\nabla p^{n+1} A_j \qquad (3.46)$$

$$\frac{1}{V}\sum_{j=1}^{N}\left(\sum_{i=1}^{Ns}\phi_{p_i}^{n+1} u_{p_i}^{n+1} A_j\right) - \frac{1}{V}\sum_{j=1}^{N}\left(\sum_{i=1}^{Ns}\phi_{p_i}^{*} u_{p_i}^{*} A_j\right) = \frac{\Delta t}{V}\sum_{j=1}^{N}\left(\frac{1}{s+C_{vm}}\sum_{i=1}^{Ns}\phi_{p_i}^{*}\right)$$

$$\nabla p^{n+1} A_j$$

$$(3.47)$$

Where V is the volume of the mesh, ϕ_d is the area fraction of all particles on the

control surface, A_j is the area of the control surface, and then the equations 3.46 and

3.47 are added together to obtain

$$\frac{1}{V}\sum_{i=1}^{Ns}\phi_{c_i}^{n+1} u_{c_i}^{n+1} A_j + \left(\sum_{i=1}^{Ns}\phi_{p_i}^{n+1} u_{p_i}^{n+1} A_j\right)] =$$

$$\frac{\Delta t}{V}\sum_{j=1}^{N}\left(\phi_{c_i}^{n} + \frac{C_{vm}}{1+\frac{C_{vm}}{s}}\sum_{i=1}^{Ns}\phi_{p_i}^{*} + \frac{C_{vm}}{s+C_{vm}}\sum_{i=1}^{Ns}\phi_{p_i}^{*}\right)\nabla p^{n+1} A_j \qquad (3.48)$$

Since 3.48 must satisfy equation 3.46, equation 3.48 can be rewritten as

$$\frac{1}{V}\sum_{j=1}^{N}\left(\phi_{c_i}^{*} u_{c_i}^{*} A_j + \left(\sum_{i=1}^{Ns}\phi_{p_i}^{n} u_{p_i}^{*} A_j\right)\right) = \frac{\Delta t}{V}\sum_{j=1}^{N}\left[\phi_{c_i}^{n} + \left(\frac{sC_{vm}+1}{s+C_{vm}}\right)\sum_{i=1}^{Ns}\phi_{p_i}^{*}\right]\nabla p^{n+1} \qquad (3.49)$$

Due to the particle type discrete individuals, so unlike the fluid type continuous flow

over the control surface of the cross-sectional area to Ap (t), as shown in Figure 3.5,

then the volume of particles through the t time V is as below

$$V_{pass} = \delta\tau \int A_p(t) u_{pi}^* A_j + \Delta t - \delta\tau \int 0 \cdot u_p^* dt \qquad (3.50)$$
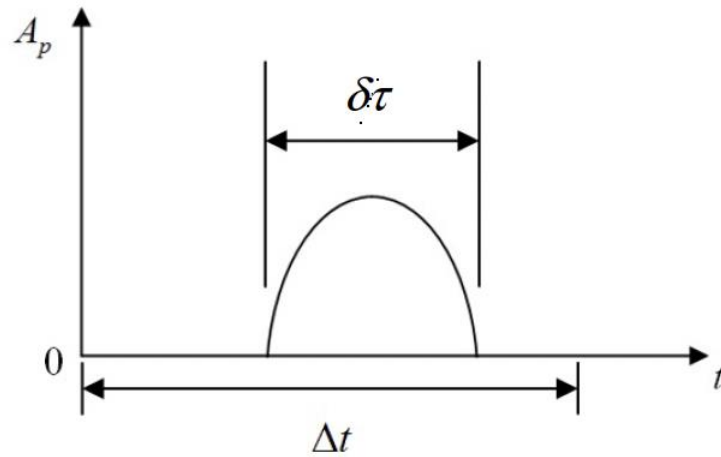
Figure 3.5 The relationship between Ap and time [7]

Where up represents the inter-particle velocity, which is constant at time t, and 1 is the

time required for the particle to pass through the control surface. And we can Ap (t)

non-zero part of the time average to Ap, as shown in Figure 3.6, the mathematical form

of 2.46 equation

$$A_p = \frac{\int A_p \, dt}{\delta\tau} \qquad (3.51)$$
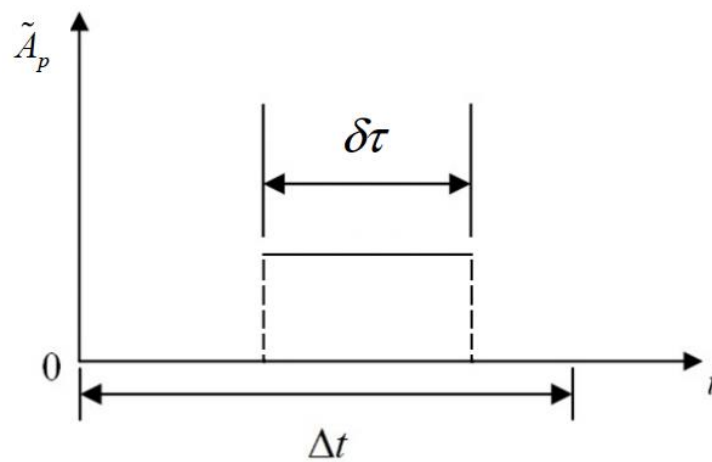
Figure 3.6 The relationship between Ap and time [7]

Therefore, V_{pass} can be expressed in the following form

58

$$V_{pass} = A_p u_p^* \delta\tau \tag{3.52}$$

The $\phi_{p_i}^*$ and $\phi_{c_i}^*$ in equation 3.49 are expressed in the following form

$$\phi_{p_i}^* = \frac{A_{pi}}{A_j} \tag{3.53}$$

$$\phi_{c_i}^* = \frac{1 - \sum_{i=1}^{Ns} A_{pi}}{A_j} \tag{3.54}$$

Substitute equations (3.53) and (3.54) into equation (3.49), and integrate the time

$$\frac{1}{V} \sum_{j=1}^{N} [(\int A_j - \sum_{i=1}^{Ns} A_{pi}) u_{c_i}^* dt + \int \sum_{i=1}^{Ns} A_{pi} u_{p_i}^* dt] = \frac{\Delta t}{V} \sum_{j=1}^{N} \{\int [(A_j - \sum_{i=1}^{Ns} A_{pi}) +$$

$$(\frac{sC_{vm}+1}{s+C_{vm}}) \sum_{i=1}^{Ns} A_{pi}] \nabla p^{n+1} dt$$

(3.54) The left side of the equal sign can be rearranged as

$$\frac{1}{V} \sum_{j=1}^{N} [\int A_j u_{c_i}^* dt + \int \sum_{i=1}^{Ns} A_{pi}(u_{pi}^* - u_{ci}^*) dt] = RHS \tag{3.55}$$

Where, after dividing the first term on the left side of equation (3.55), we get

$$\int A_j u_{c_i}^* dt = u_{c_i}^* A_j \Delta t \tag{3.56}$$

And the second item can be expanded into

$$\int \sum_{i=1}^{Ns} A_{pi}(u_{pi}^* - u_{ci}^*) dt = \int [A_{p1}(u_{p1}^* - u_{cj}^*) + A_{p2}(u_{p2}^* - u_{cj}^*) + \ldots] dt. \tag{3.57}$$

Integrating equation (3.56) yields

$$\int \sum_{i=1}^{Ns} A_{pi}(u_{pi}^* - u_{ci}^*) dt = A_{p1}(u_{p1}^* - u_{cj}^*) \delta\tau_1 + A_{p2}(u_{p2}^* - u_{cj}^*) \delta\tau_2 + \ldots \tag{3.58}$$

Substituting equation 3.52 into equation 3.58, we get

$$\int \sum_{i=1}^{Ns} A_{pi}(u_{pi}^* - u_{ci}^*) dt = \frac{V_{pass1}}{u_{p1}^*}(u_{p1}^* - u_{cj}^*) + \frac{V_{pass1}}{u_{p2}^*}(u_{p2}^* - u_{cj}^*) + \ldots \tag{3.59}$$

After finding the total volume flowing over the control surface by equations 3.56 and

3.59, substituting into equation 3.55, we get

59

$$\frac{1}{V}\sum_{j=1}^{N}[\ u_{cj}^{*}A_{j}\Delta t+\frac{V_{pass1}}{u_{p1}^{*}}(u_{p1}^{*}\text{-}u_{cj}^{*})+\frac{V_{pass2}}{u_{p2}^{*}}(u_{p2}^{*}\text{-}u_{cj}^{*})+....]= RHS \tag{3.60}$$

The right-hand side of the equal sign of Eq (3.61) can be organized as follows

$$LHS=\frac{\Delta t}{V}\sum_{j=1}^{N}\{\int[\ A_{j}+\frac{(1-s)(1-C_{vm})}{s+C_{vm}}\sum_{i=1}^{Ns}A_{pi}\ ]dt\}\nabla p^{n+1} \tag{3.61}$$

Decomposing the integrals in parentheses of Eq. (3.62) yields

$$LHS=\frac{\Delta t}{V}\sum_{j=1}^{N}\{\int A_{j}\ dt+\frac{(1-s)(1-C_{vm})}{s+C_{vm}}\sum_{i=1}^{Ns}A_{pi}\ dt\ \}\nabla p^{n+1} \tag{3.62}$$

From equations 3.51 and 3.52, it follows that

$$\int A_{j}dt=\frac{V_{pass\ i}}{u_{pi}^{*}} \tag{3.63}$$

Substituting equation (3.63) into equation (3.58) yields

$$LHS=\frac{\Delta t^{2}}{V}\sum_{j=1}^{N}[1+\frac{(1-s)(1-C_{vm})}{s+C_{vm}}\sum_{i=1}^{Ns}\frac{V_{pass\ i}}{u_{pi}^{*}A_{j}\Delta t}]\ \nabla p^{n+1}A_{j} \tag{3.64}$$

Then by collapsing Eqs. (3.60) and (3.64), we get

$$\frac{1}{V}\sum_{j=1}^{N}[\ u_{cj}^{*}A_{j}\Delta t+\sum_{i=1}^{Ns}\frac{V_{pass\ i}}{u_{pi}^{*}}(u_{pi}^{*}-u_{cj}^{*})]=\frac{\Delta t^{2}}{V}\sum_{j=1}^{N}[1+\frac{(1-s)(1-C_{vm})}{s+C_{vm}}\sum_{i=1}^{Ns}\frac{V_{pass\ i}}{u_{pi}^{*}A_{j}\Delta t}](3.65)$$

(3.65) is the pressure equation for the solid-liquid system model of this study.

Considering that the particles move in three stages, it is not possible to solve the

pressure field by summing up the fluxes on all control surfaces and solving the poisson

equation once, as in the original mapping method.

In this study, the pressure field is first solved by the volume flux caused by the

fluid, and a correction step is made with the particle transport. Then let the particles

move in one direction, calculate the volume flux of the particles in that direction, then

solve the dynamic pressure equation once, make a correction step with the resulting
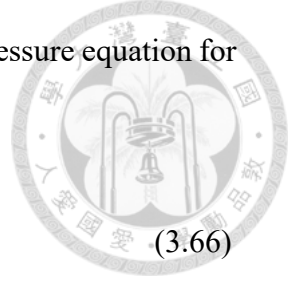
pressure, then continue to move the particles, and so on, solve the pressure equation for four times, that is, disassemble the equation 3.60 as follows

$$\frac{1}{V}\sum_{j=1}^{N}u_{cj}^{*}A_{j}=\frac{\Delta t}{V}\sum_{j=1}^{N}\left[\phi_{c_{i}}^{n}+\frac{(sC_{vm}+1)}{s+C_{vm}}\sum_{i=1}^{Ns}\phi_{p_{j}}^{n}\right]\nabla p_{1}^{n+1} \tag{3.66}$$

$$Flux_{px}=\frac{\Delta t^{2}}{V}\sum_{j=1}^{N}\varphi\,\nabla p_{2}^{n+1} \tag{3.67}$$

$$Flux_{py}=\frac{\Delta t^{2}}{V}\sum_{j=1}^{N}\varphi\,\nabla p_{3}^{n+1} \tag{3.68}$$

$$Flux_{pz}=\frac{\Delta t^{2}}{V}\sum_{j=1}^{N}\varphi\,\nabla p_{3}^{n+1} \tag{3.69}$$

Which,

$$\varphi=1+\frac{(1-s)(1-C_{vm})}{s+C_{vm}}\sum_{i=1}^{Ns}\frac{V_{pass\,i}}{u_{pi}^{*}A_{j}\Delta t} \tag{3.70}$$

Since the position of the particles will change every time the pressure equation is solved, it is necessary to do the correction step immediately, and the liquid phase must be corrected together, if the one-dimensional situation is illustrated, i.e., equations (3.27) and (3.29) are disassembled again as follows

$$u_{c}^{**}=\frac{\phi_{c}^{n}}{\phi_{c}^{**}}u_{c}^{*}-\frac{\Delta t}{\phi_{c}^{**}}\left(\phi_{c}^{n}+\frac{C_{vm}\phi_{d}^{n}}{1+\frac{C_{vm}}{s}}\right)\nabla p_{1}^{n+1} \tag{3.71}$$

$$u_{c}^{n+1}=\frac{\phi_{c}^{**}}{\phi_{c}^{n+1}}u_{c}^{**}-\frac{\Delta t}{\phi_{c}^{n+1}}\left(\phi_{c}^{n}+\frac{C_{vm}\phi_{d}^{n}}{1+\frac{C_{vm}}{s}}\right)\nabla p_{2}^{n+1} \tag{3.72}$$

$$u_{p}^{**}=u_{p}^{*}-\frac{\Delta t}{s+C_{vm}}\nabla p_{1}^{n+1} \tag{3.73}$$

$$u_{p}^{n+1}=u_{p}^{**}-\frac{\Delta t}{s+C_{vm}}\nabla p_{2}^{n+1} \tag{3.74}$$

After obtaining up from Eq. (3.73), a particle transport is carried out to obtain u_{p}^{**}, and then ϕ_{c}^{**}, u_{c}^{n+1}, and u_{p}^{n+1} are substituted into Eq (3.71) to obtain u_{c}^{**}, and so on, and finally u_{c}^{n+1} and u_{p}^{n+1} can be obtained.

61

3.4 Fluid Properties
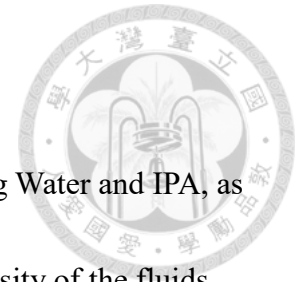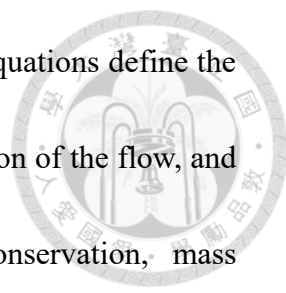
The fluids used in this study were two types of fluids, including Water and IPA, as shown in the table, which contains the properties, density and viscosity of the fluids.

Table 3.1 Fluid Properties

Fluid	Water	IPA
Density	$998.2 kg/m^3$	$786 kg/m^3$
Velocity	0.2 m/s, 0.3 m/s, 0.39 m/s, 1 m/s, 5 m/s	0.2 m/s, 0.3 m/s, 0.39 m/s, 1 m/s, 5 m/s
Kinematic Viscosity	0.890 cP	2.86 cP
Particle number	500	500
Particle type	Silica	Silica
Concentraction	500/500ml	500/500ml
Particle size	20nm	20nm
Wall	bounce	bounce

3.5 COMSOL Multiphysics Calculator and Related Calculations

In this study, the experiments in the article of Miglozzi rt al [6] are used as a prototype, and the numerical analysis of the transient three-dimensional flow field model is assisted by the finite element method simulation software, COMSOL Multiphysics [12,13], which integrates the tools for describing the different types of

fluid flow and can be used in simple interfaces whose underlying equations define the momentum conservation, mass conservation, and energy conservation of the flow, and therefore the underlying equations define the momentum conservation, mass conservation, and energy conservation of the flow, and therefore the underlying equations define the momentum conservation, mass conservation, and energy conservation of the flow. The underlying equations of these interfaces define the conservation of momentum, mass, and energy of fluid flow, and therefore COMSOL Multiphysics can be used to calculate steady or transient problems for geometries of different dimensions, as well as linear or nonlinear problems of the flow field. The interface remains flexible and easy to use, and the ability to edit expressions of functions composed of model variables, to define material properties, to adjust the density and position of the mesh, etc., has made it one of the most popular software in many research and industrial applications today.

(1) Select the dimension in which the flow field problem is to be solved and its physical correlation assumptions.

(2) Trace the geometry. In this study, we use the built-in COMSOL drawing software to build the mechanism.

(3) Setting parameters and variables.

(4) Setting up the study material properties.

(5) Set the initial and boundary conditions of the problem.

(6) Create a grid. COMSOL's built-in grid allows you to choose from five levels of coarseness and fineness or define your own, as well as regional grid refinement.

(7) Calculation and post-processing.

Chapter 4 RESULTS and DISCUSSIONS
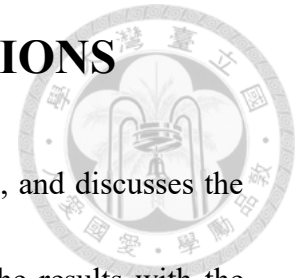
This chapter discusses the mesh setup in Comsol Mutiphysics, and discusses the simulation results of water and IPA respectively, and compares the results with the experiments to investigate the results under different parameters. The study simulates three more complex mechanisms as shown in Figure 4.1, Figure 4.2, Figure 4.3, where Figure 4.2 is the valve designed for the present study, which is referred to as type 2, Figure 4.1 and Figure 4.3 are referred to as type 1 and type 3, where type 1 and type 3 are the valves that have been used in the past and type 2 is designed to improve the particle buildup. In type1 and type3, the valves were used in the past, while type 2 was designed to improve the particle accumulation, the geometry and dimensions are shown in Fig. The following valves were designed for this study, which required a larger mesh system and different mesh scales.

We tried a million-level mesh (67,953,90 finite elements) for the calculation, and found that there is still room for improvement in the clarity, and then we used a ten-million-level mesh (42,301,300 finite elements), as shown in Figure (4.2), and then we got a better result. In COMSOL, the spatial discretization of the computational domain was performed using triangular elements with a maximum element size of 0.75 mm, a minimum element size of 0.075 mm, and a curvature factor of 0.25. The maximum element size was 0.75 mm and the minimum element size was 0.075 mm.

65

Figure 4.1 3D model of type 1 valve   Figure 4.2 3D model of type 2 valve
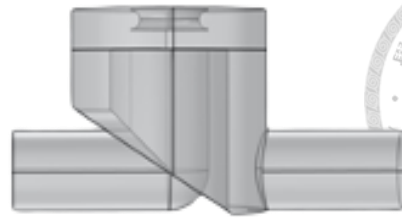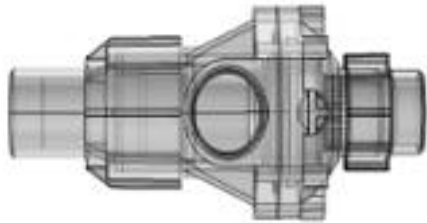
Figure 4.3 3D model of type 3 valve

Figure 4.4 Mesh of type 1 valve
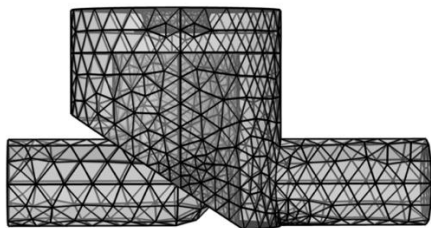
Figure 4.5 Mesh of type 2 valve   Figure 4.6 Mesh of type 2 valve
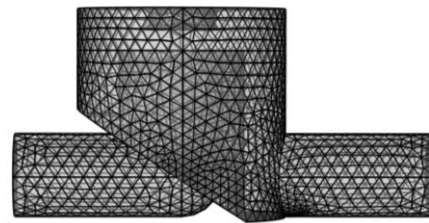
In COMSOL software, there are 9 built-in network modes, based on normal, there are 4 levels of coarsening or thinning, and for thinning, there are "Normal, Thinning, More Thinning, Special Thinning, Extreme Thinning," After several tests, the final mesh selected is the "Thinning" mode of the built-in mesh in COMSOL, and the mesh

66

shape used is set to be triangular, and we have also attempted to carry out the simulation

calculations under the "Thinner" mode, and it took us about 2-3 times longer, and

weighed it out, and it is more time-consuming to use the "Thinning" mode.
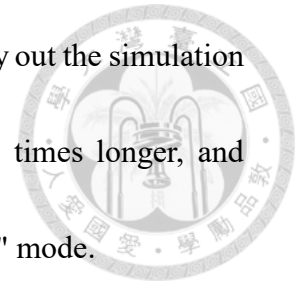
4.1 Simulation Results of Newtonian Fluid

In this section, the flow field development of Newtonian fluid through the valve is

investigated and analyzed numerically using particle tracking method and compared

with the experimental results. Figures 4.7 and 4.8 show that the fluid is water, the feed

velocity is 0.3m/s and 0.39m/s for type 1 valves, where the red area is the faster area
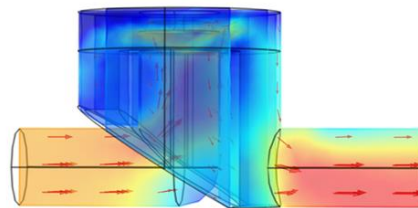
and the blue area is the slower area.
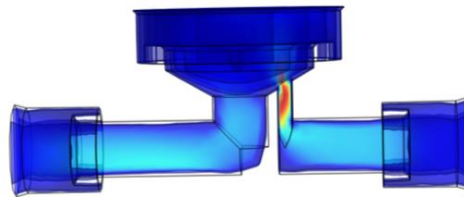
Figure 4.7 Fluid simulation (Water) of type 1 valve with velocity 0.3m/s
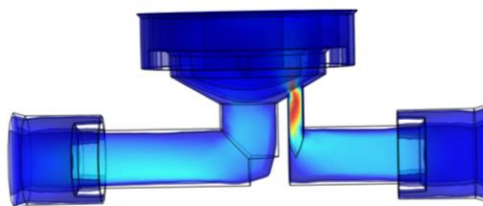
Figure 4.8 Fluid simulation (Water) of type 1 valve with velocity 0.39m/s

From Figure 4.7 and Figure 4.8 the left side of the inlet port, the right side of the outlet

port, the valve does not look like the pipe conveying a large amount of conveying

distance is long, conveying speed is higher, after the test, the three types of valves using

67

the speed of less than 1m/s has a better particle penetration rate, less particle

accumulation in the valve, from the two charts, the speed is more than the average.
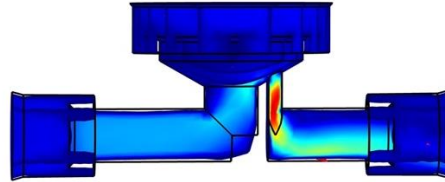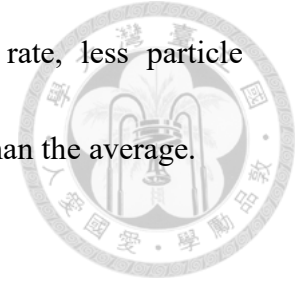
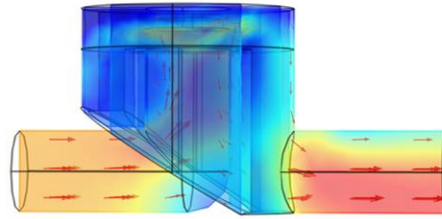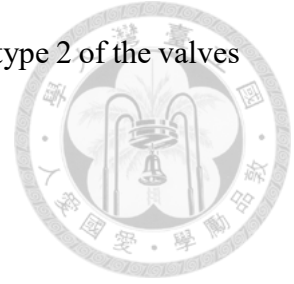Figure 4.9 Fluid simulation (IPA) of type 1 valve with velocity 0.3m/s
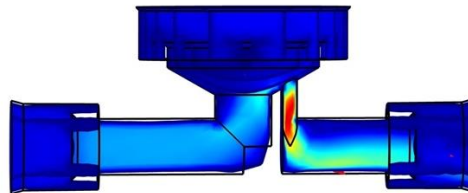
Figure 4.10 Fluid simulation (IPA) of type 1 valve with velocity 0.39m/s

Fig. 4.9 Flow field change in the valve element for IPA with velocity 0.3m/s.4.10

Flow field for IPA with velocity 0.39m/s.

Figure 4.9 and Figure 4.10 Fluid for IPA, feed velocity of 0.3m/s and 0.39m/s in Type

1 valve, where the red area is the faster area, the blue area is the slower speed, the

difference between the feed IPA and water in the Figure 4.9 and Figure 4.10 the

downstream end of the flow velocity is faster.
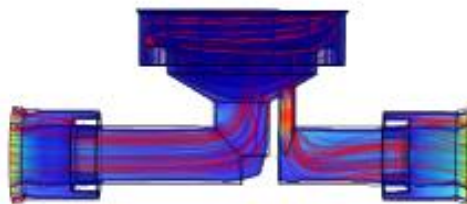
Figure 4.11 Streamline of type 1 valve with velocity 0.3m/s
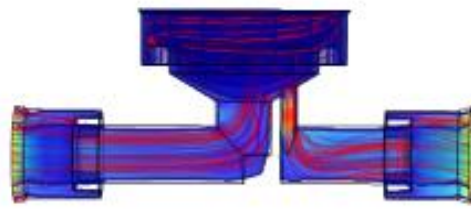
Figure 4.12 Streamline of type 1 valve with velocity 0.39m/s

Figures 4.11 and 4.12 show type 1 valves for IPA with feed velocities of 0.3 m/s and 0.39 m/s, respectively.

From the streamline diagram, although the streamline is average, the exit position is faster, but only in the particle tracking to see in which position the accumulation.

Figure 4.13 Fluid simulation (Water) of type 2 valve with velocity 0.3m/s
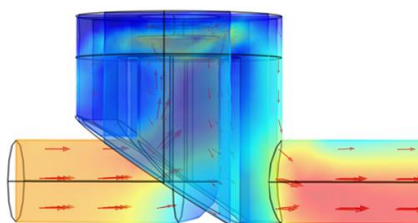
Figure 4.14 Fluid simulation (Water) of type 2 valve with velocity 0.39m/s

Figure 4.13 the fluid is water, the velocity is 0.3m/s, and Figure 4.14 the fluid is water,

69

the velocity is 0.39m/s, the red area is slower, the blue area is faster, type 2 of the valves

of the two flow field distribution is not very different.

Figure 4.15 Fluid simulation (IPA) of type 2 valve with velocity 0.39m/s
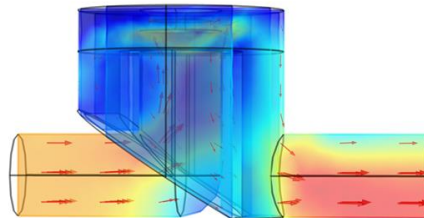
Figure 4.16 Fluid simulation (IPA) of type 2 valve with velocity 0.39m/s

Figure 4.15 the fluid is water, the velocity is 0.3m/s, and Figure 4.16 the fluid is IPA,

the velocity is 0.39m/s, the red area is slower, the blue area is faster, the type 2 valves

are not much difference in the distribution of the two flow fields.
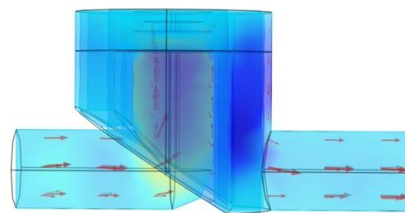
Figure 4.17 z-component velocity field of type 2 valve
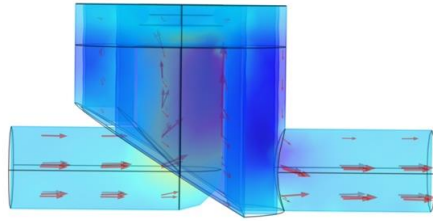
Figure 4.18 z-component velocity field of type 2 valve

Because of the simulation of different fluids, including water and IPA, because from Figure 4.13 to 4.16 can not see too much difference, from the point of view of the flow field simulation, to take out **the Z component** of the velocity field, from Figure 4.17 and 4.18 can be seen in 4.18 fluids for the IPA, there is a more upward component, which can lead to the particle motion.
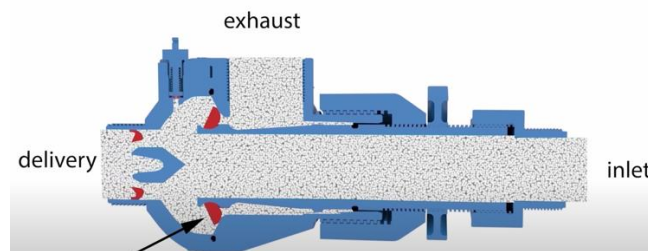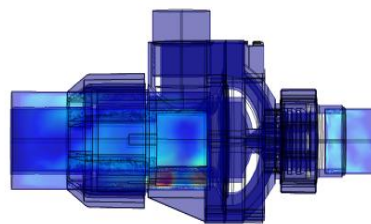

Figure 4.19 3D model of type 3 valve

Figure 4.20 Fluid simulation of type 3 valve with open state

71
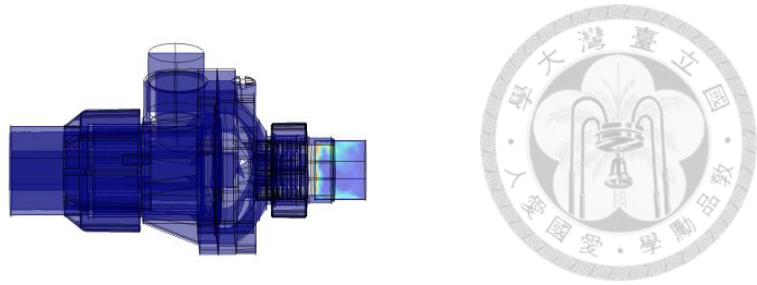
Figure 4.21 Fluid simulation of type 3 valve with close state

4.2 Particle Tracking Method

In this study, the Lagrangian description method is used to analyze the motion of particles, that is, the particles are regarded as discrete individuals and the movement of particles is chased one by one. Therefore, one of the key points of this numerical model is how to transfer the particles between the grids correctly.

Based on the independence of the motion, we split the particle movement into three orthogonal directions in the Cartesian coordinates, and the sequence of the different movements has no effect. The reason for splitting the particle movement into three is that if the particle movement is controlled to be no more than one grid distance, then each grid will only need to take into account the information of one grid before and one grid after it, which is similar to the Eulerian Adection scheme, and it is much simpler than moving to the position in one go. Another consideration is that the flux of the particles on the control surface is needed for the subsequent calculation, and it is easier to calculate the number of particles passing on the control surface by moving in three directions to find the flux of the particles.

72
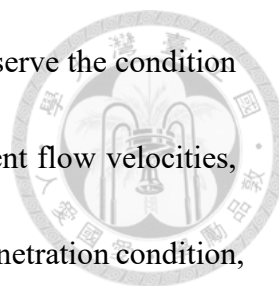
Particle tracking method, i.e., put fluid particles at the inlet to observe the condition of the flow field, this subsection calculates the flow field at different flow velocities, and will be 500/ml of particles into the inlet to observe the particle penetration condition, the simulation results are shown in Figure 4.22 and Figure 4.23 for the speed = 0.39m/s, the fluid is IPA, you can see that there is a buildup of particles, and then we will utilize the particles to quantify the particles. Then we will use the particle quantification tool Accumulator to calculate the flow rate at 0.39 and in our design type 2 valves have the least accumulation of particles.
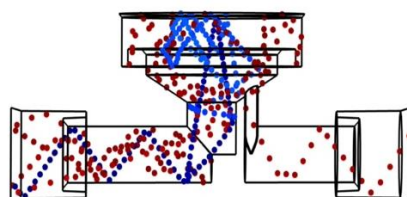
Figure 4.22 Particle tracking (Water) of type 1 valve with velocity 0.3m/s
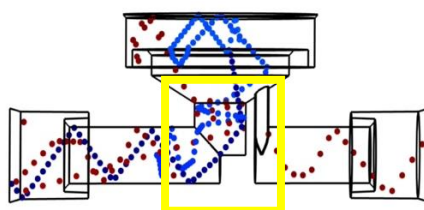

Figure 4.23 Particle tracking (Water) of type 1 valve with velocity 0.39m/s

Fig. 4.22 and 4.23, the fluid is water, the speed is 0.39m/s, the total time required is 8s, Fig. 4.22 is the position of the particles at the time of 4s, Fig. 4.23 is the state of the particles at the time of 8s after running all the particles, it can be found that the particles

are piled up in the bottom of the curved pipe, and it is presumed that it is possible to be

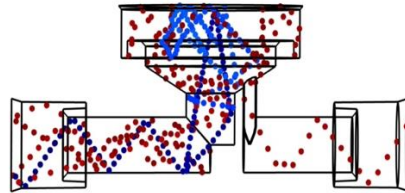a larger number of vortexes at the position.

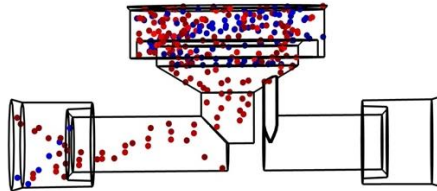Figure 4.24 Particle tracking (IPA) of type 1 valve with velocity 0.3m/s

Figure 4.25 Particle tracking (IPA) of type 1 valve with velocity 0.39m/s

Figure 4.24 and 4.25 fluid for IPA, speed of 0.39m/s, the total time required for 8s,

Figure 4.24 for the location of the particles at 4s, Figure 4.25 for the particles in the run

through all the particles, the state of the 8s, you can find particles in the upper surface

of the pile up, it is possible to speculate that the turbulence for the greater number of

the location, and also because of viscous liquids more able to drive the particle

movement, 8s to the particles above the valve parts of the pile. The particles are brought

to the top of the valve at 8s.

Table 4.1 The relationship of Penetration rate and Velocity of type 1 valve

Velocity (m/s)	Step length (s)	No. of particles penetration through the valve	Penetration rate (%)	No. of particles penetration through the valve in experiment
0.2	8	382	76.4	377
0.30	8	390	78	385
0.39	8	402	80.4	396
1.0	8	376	75.2	363
5.0	8	361	72.2	349

In Table 4.1, the fluid is water, it can be seen that with the increase of velocity, the particle penetration rate will be reduced, in the velocity of 0.39 is the best penetration rate of the flow.
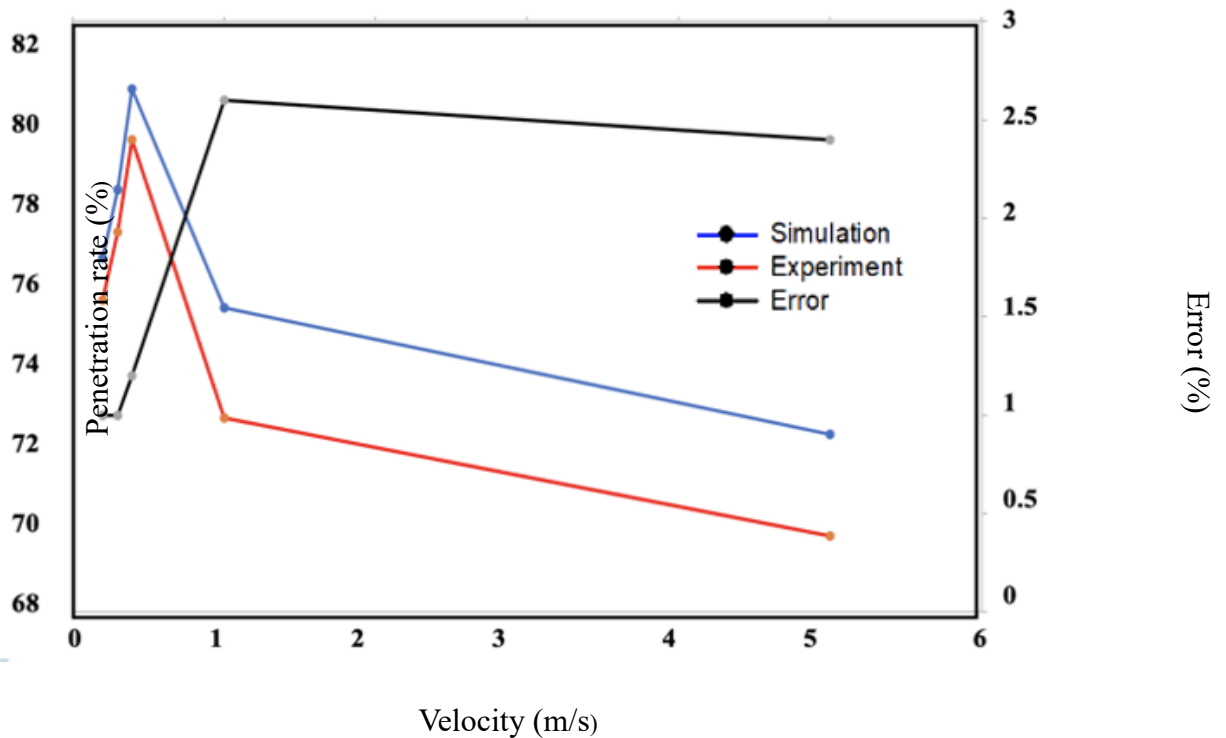
Figure 4.26 The relationship of Penetration rate and Velocity

Table 4.2 The relationship of Penetration rate and Velocity of type 1 valve

Velocity (m/s)	Step length (s)	No. of particles penetration through the valve	Penetration rate (%)	No. of particles penetration through the valve in experiment
0.2	8	401	80.2	396
0.30	8	409	81.8	407
0.39	8	422	84.4	418
1	8	397	79.4	391
5	8	383	76.6	371

In Table 4.2, the fluid is IPA, we can see that as the velocity increases, the particle

penetration rate decreases, and the velocity of 0.39 is the best penetration rate.
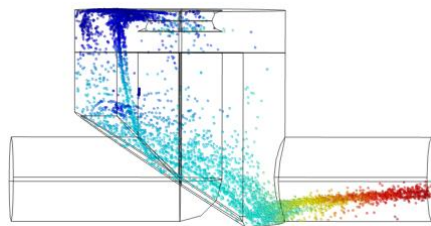
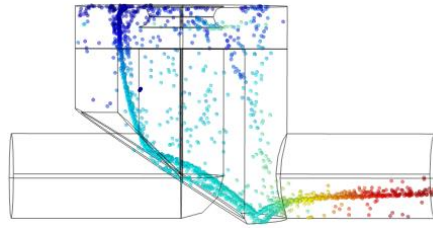Figure 4.27. Particle tracking (IPA) of type 2 valve with velocity 0.39m/s

Figure 4.28 Particle tracking (IPA) of type 2 valve with velocity 0.39m/s

In Figures 4.27 and 4.28, in order to investigate whether different fluids have different

effects on particle accumulation, the difference between two different fluids lies in the

viscosity, therefore, the particle tracking method is used to observe the state of water

and IPA at 3.5s, and the velocity of the water is 0.39m/s. It can be found that the distance

of the IPA-driven particles is larger than that of water.
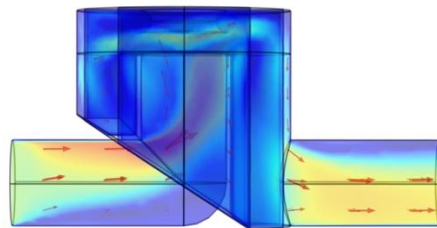

Figure 4.29 Fluid simulation of type 2 valve under 1m/s
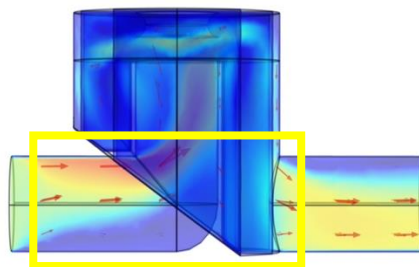

Figure 4.30 Fluid simulation of type 2 valve under 5m/s

Figures 4.29 and 4.30, the flow rate of 1m/s and 5m/s respectively, it can be found that

if the flow rate of the feed material is too fast, it will be rushed to the top of the valve

part directly, and it is assumed that due to this factor, the accumulated particles can not

77

be taken away from the bottom of the valve part, and thus the particle penetration rate
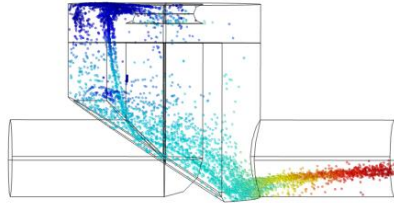
is poor.

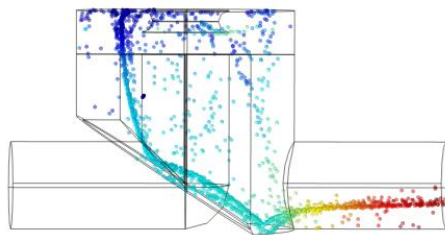Figure 4.31 Particle tracking of type 2 valve at t=3.5s

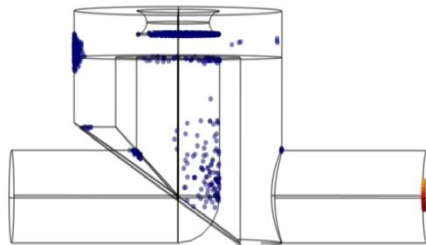Figure 4.32 Particle tracking of type 2 valve at t=4s

Figure 4.33 Particle tracking of type 2 valve at t=8s

In Figs. 4.31, 4.32, 4.33, using particle tracking to observe the velocity of 0.39m/s, the

fluid is IPA, at t=3.5s, 4s 8s the position of the particles, from the observation that the

use of type 2 designed valves, the accumulation of particles, compared with type 1 has

been greatly improved.

78

Table 4.3 The relationship of Penetration rate and Velocity of type 2 valve

Velocity (m/s)	Step length (s)	No. of particles penetration through the valve	Penetration rate (%)	No. of particles penetration through the valve in experiment
0.2	8	429	85.8	427
0.3	8	442	88.4	437
0.39	8	454	90.8	450
1	8	411	82.2	400
5	8	386	77.2	375

In Table 4.3, the fluid is water and the valve is type 2, it can be seen that with the increase of speed, after the speed 1m/s, the particle penetration rate will be reduced, in the speed 0.39m/s is the best penetration rate of the flow velocity, type 2 in the penetration rate are better than type 1 valve.

Table 4.4 The relationship of Penetration rate and Velocity of type 2 valve

Velocity (m/s)	Step length (s)	No. of particles penetration through the valve	Penetration rate (%)	No. of particles penetration through the valve in experiment

79

0.2	8	447	89.4	---
0.3	8	455	91	452
0.39	8	462	92.4	460
1	8	423	84.6	421
5	8	397	79.4	393

In Table 4.4, the fluid is IPA and the valve is type 2, it can be seen that with the increase of speed, after the speed 1m/s, the particle penetration rate will be reduced, in the speed 0.39m/s is the best penetration rate of the flow velocity, type 2 in the penetration rate are better than type 1 valve.
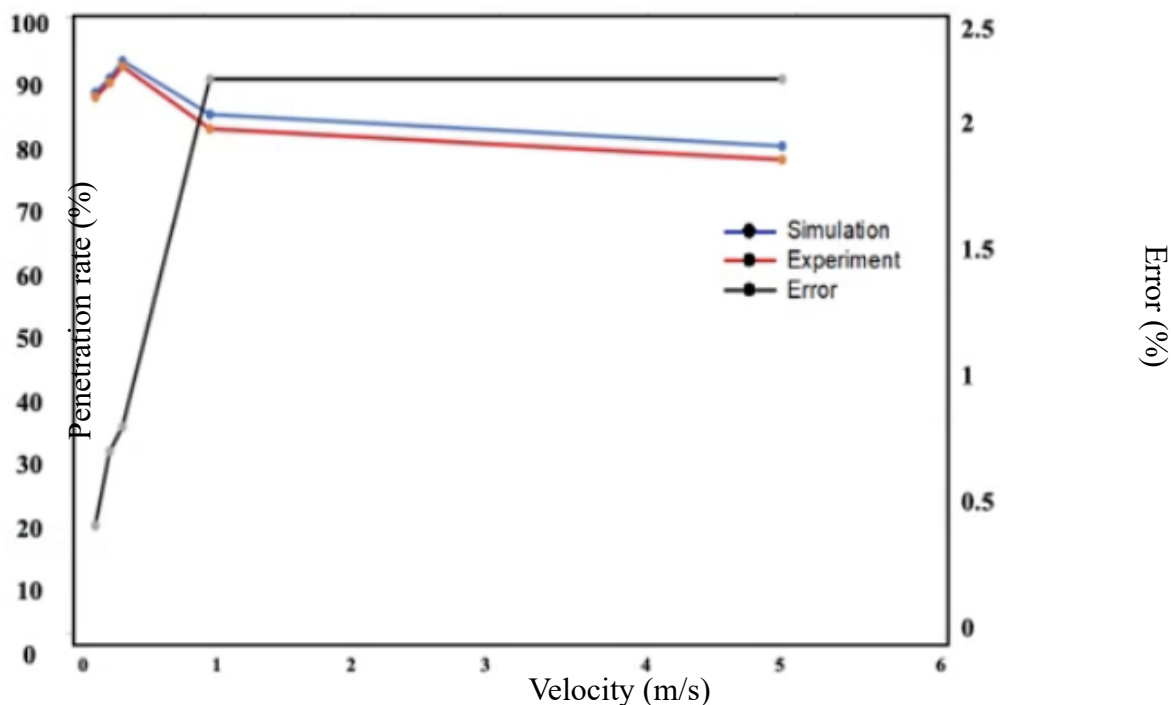

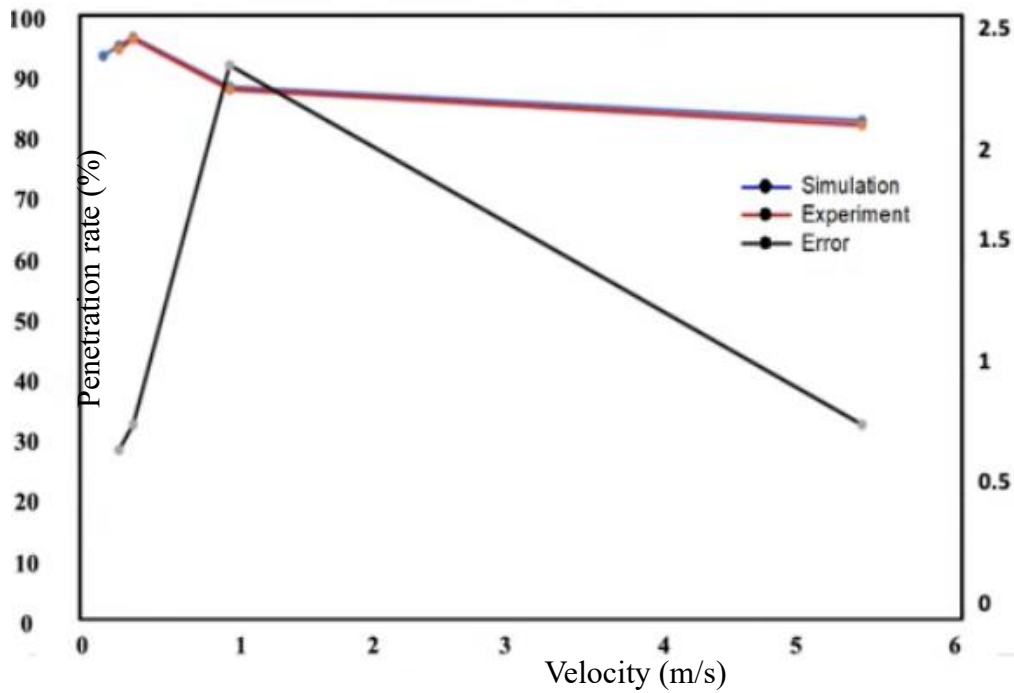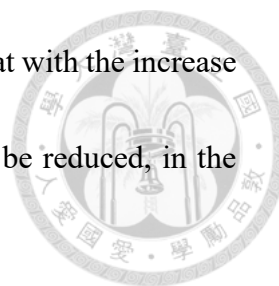Figure 4.34 The relationship of Penetration rate and Velocity

Figure 4.35 The relationship of Penetration rate and Velocity

Table 4.5 The relationship of Penetration rate and Velocity of type 3 valve

Velocity (m/s)	Step length (s)	No. of particles penetration through the valve	Penetration rate(%)
0.2	8	411	82.2
0.3	8	420	84
0.39	8	422	84.4
1	8	402	80.4
5	8	387	78

81

In Table 4.5, the fluid is water, the valve is type 3, we can see that with the increase of speed, after the speed of 1m/s, the particle penetration rate will be reduced, in the speed of 0.39m/s is the best penetration rate of the flow rate.

Table 4.6 The relationship of Penetration rate and Velocity of type 3 valve

Velocity (m/s)	Step length (s)	No. of particles penetration through the valve	Penetration rate(%)
0.2	8	414	82.8
0.3	8	424	84.8
0.39	8	426	85.2
1	8	407	81.4
5	8	393	78.6

In Table 4.6, the fluid is IPA, the valve is type 3, we can see that with the increase of speed, after the speed of 1m/s, the particle penetration rate will be reduced, in the speed of 0.39m/s is the best penetration rate of the flow rate.
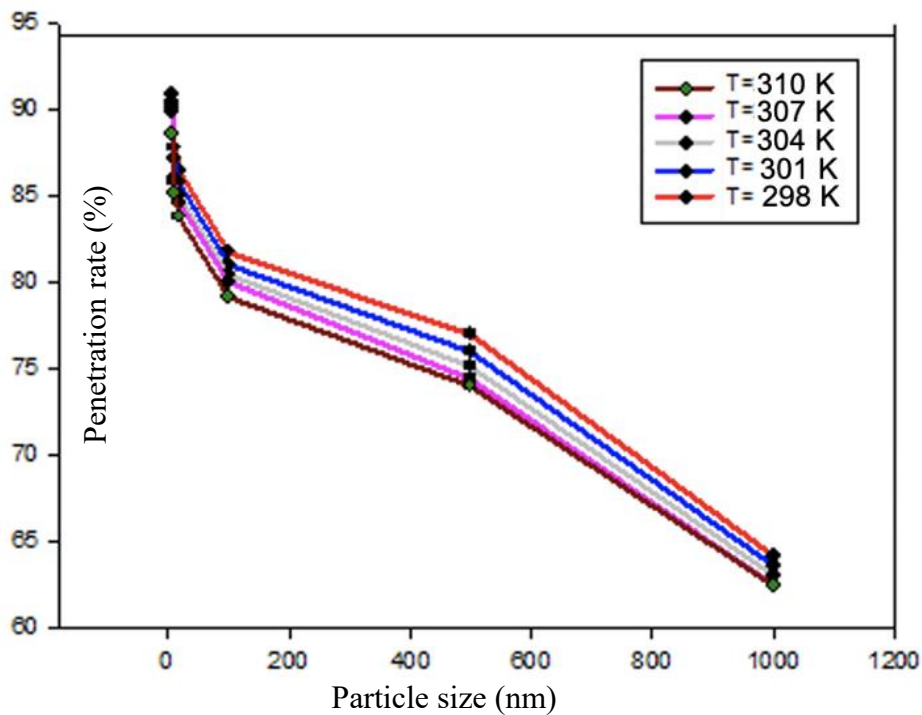
Figure 4.36 The relationship of Penetration rate and Particle size with velocity

0.39m/s

In Figures 4.36, the valve is type 2, and the feed liquid is IPA, we want to explore

whether the temperature and particle size affect the particle penetration rate, from

Figure (4.36), we can see that the flow rate of the feed material is fixed at 0.39m/s, with

the increase of the temperature, the viscosity will be reduced, and the particle

penetration rate will be reduced, we can know that viscosity will affect the particle

stacking, from the figure, we can also see that with the increase of particle size, the

particle penetration rate is reduced. affect the accumulation of particles, from the figure

can also be seen with the increase in particle size, particle penetration rate decreases.
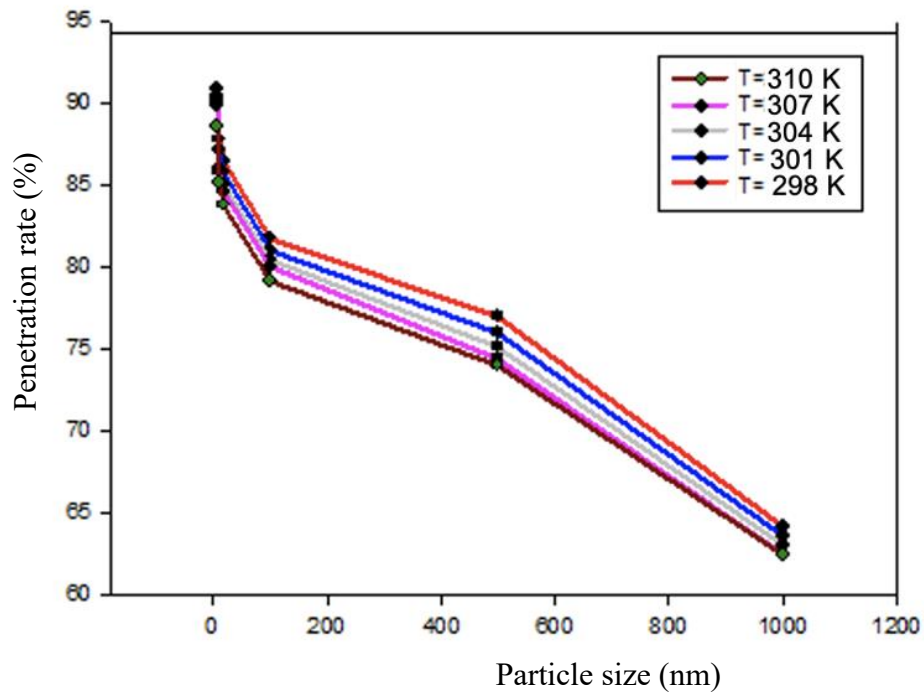
83

Figure 4.37 The relationship of Penetration rate and Particle size with velocity 0.3m/s

From the figure 4.37 can see the feed flow rate is fixed at 0.3m/s, with the temperature increase, the viscosity will be reduced, the particle penetration rate will also be reduced, from this we can know that the viscosity will affect the particle stacking, from the figure can also be seen with the increase in the size of the particles, the particle penetration rate decreases.
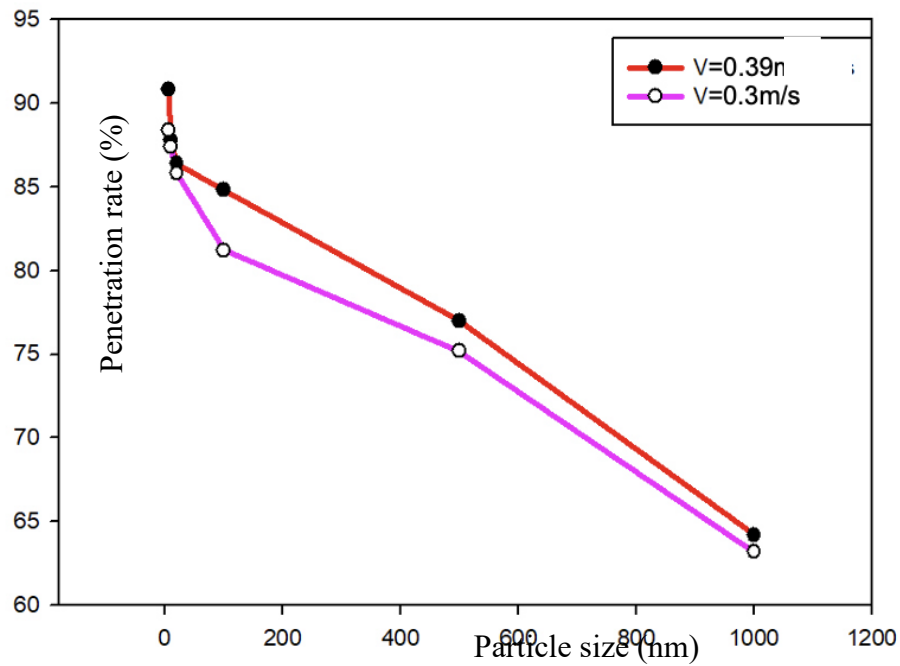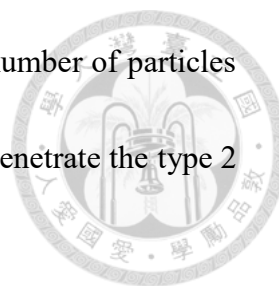
Figure 4.38 The relationship of Penetration rate and Particle size

From Fig. (4.38), it can be seen that there is a better particle penetration rate when the velocity is 0.39 m/s.

Table 4.7 The relationship of Penetration rate and Particle number

Particle numbers	Velocity (m/s)	Particle size (nm)	No. of particles penetration through the valve	Penetration rate (%)
500		20	454	90.8
1000		20	910	91.0
1500	0.39	20	1368	91.2
2000		20	1837	91.8
3000		20	2768	92.2

In Table 4.7, by dropping 20nm particles, we can see that the number of particles changes, and when the number of particles increases, the particles penetrate the type 2 valves with less buildup and higher penetration rate.

4.3 Other methods to Improve Particle Deposited

Table 4.8 The relationship of Penetration rate and Velocity by changing chamfer

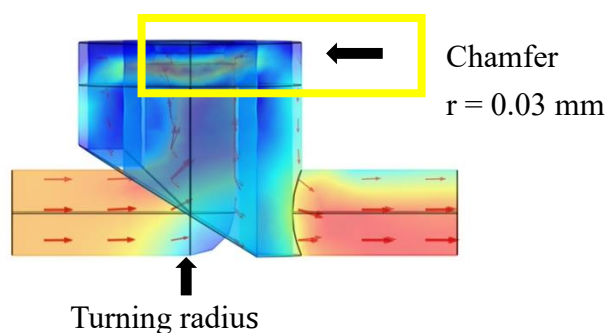| Velocity (m/s)	Step length (s)	No. of particles penetration through the valve	Penetration rate (%)
0.2	8	429	85.8
0.30	8	440	88.8
0.39	8	454	90.8
1	8	414	82.8
5	8	390	78.8

Figure 4.39 3D model of type 2 valve

86

In this section of the study, from the design of chamfered or rounded corners into the Type2 valve, hoping to enhance the particle penetration rate, so that the purity of the chemical products and then enhance the design of the valve above the chamfer, the design of r = 0.03mm, but from the Table4.8, the penetration rate of the particles are to enhance the design of valves, so the design of the valve turned to the bottom of the turing radius.
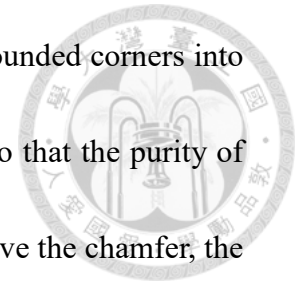
Table 4.9 The relationship of Penetration rate and Velocity by changing turning radius

Turning radius R (mm)	The pressure loss (Pa)	Penetration rate (%)
1.00	2179	90
0.90	2127	91.2
0.85	1984	91.6
0.80	1778	92.2
0.75	1752	92.2
0.7	2191	87.2

Table 4.10 3D Printing Parameters

Material	HDT80	HDT80	HDT80
Layer Height	0.2mm	0.2mm	0.2mm
Line Width	0.4mm	0.4mm	0.4mm
Wall Line Width	0.4mm	0.4mm	0.4mm
Wall Thickness	1mm	1mm	1mm
Withdrawal Speed	70mm/s	80mm/s	90mm/s
Printing Temperature	100°C	100°C	100°C

Figure 4.40 3D printing model

Table 4.11 The relationship of Penetration rate and Velocity between experiment and

simulation

Velocity (m/s)	Step Length (s)	No. of particles penetration through the valve in experimental by using original material	No.of particles penetration through the valve in experimental by using new material

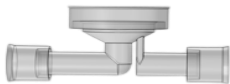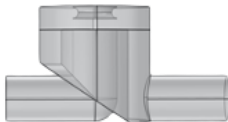|			
0.3	8	444	452
0.39	8	452	460
1	8	413	421
5	8	388	393
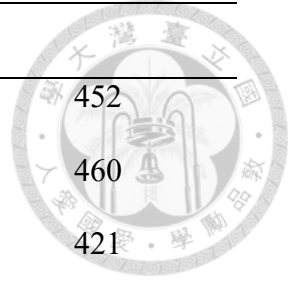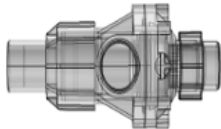
Table 4.12 Comparison of 3 types of valves

Name	Type 1 Valve	Type 2 Valve (Improved Valve)	Type 3 Valve
Production method	Injection Molding	3D printing	Injection Molding
Accumulation place	Above the valve	Above the valve and pipe bend	Above the valve
Penetration Rate (Water) with velocity=0.39m/s	80.4%	90.8%	84.4%
Penetration Rate (IPA) with velocity=0.39m/s	84.4%	92.4%	85.2%
Advantages	1.Low resistance 2.Simple Structure	1.Low resistance 2.Simple Structure	1.Fluid cut off 2.Good flow control
Penetration Rate(%)	Normal	The best	Best

Chapter 5 CONCLUSIONS
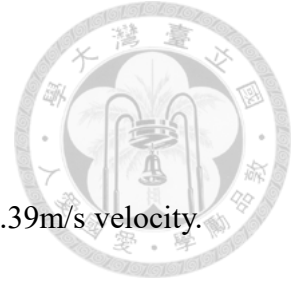
1.The type 2 Valve exhibited great Penetration Rate(~90%) ,using 0.39m/s velocity.

2. The technology has the potential for improving quality. For example, through 3-D printed valve, producing clean products

3. AM leaves a smaller environmental footprint. The

technology generates little waste as only the needed materials are used(Ex:HDT80) .

4. High-viscosity fluids are better able to drive particles in valve.

5. As the liquid temperature increases, it will reduce the viscosity, research has learned that high viscosity is more able to drive the particle movement, if you use a lower viscosity fluid, you can reduce the temperature, enhance the particle penetration rate.

6. In this study found that the more the number of particles will enhance the particle penetration rate, reduce the particles in the valve parts in the accumulation, presumably because the original particle accumulation has been stacked particles, particles were ejected.

7. The particle transport system used in this model stores discrete particles on a Yola grid, so that if a particle needs to use grid information in its calculation, it can immediately obtain information from the surrounding grids. By dividing the movement of the particles into three directions and controlling that the particles do

not move more than one grid at a time, the process of receiving particles on the grid

and calculating the particle volume flux can be greatly simplified, as only the

information from the previous and next grids need to be taken into account.
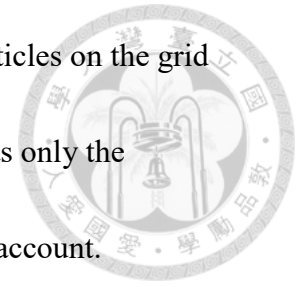
8. Instead of continuing the solid-liquid two-phase flow with the solid-air system

assumption, we reconsider the dynamic pressure gradient and the additional mass

effect, which have been neglected due to the density difference, into the equations of

motion of the particles. Through the momentum exchange between phases, the

momentum equation of solid-liquid two-phase flow is expressed in the form of a

system, and through the operation of the inverse matrix, the additional mass term can

be disassembled into the components of the other forces, thus simplifying the

numerical calculation.

9. In the design concept, it was found that there would be the least amount of particle

buildup when the inclined plate tended to be at 45 degrees.

REFERENCES

[1] Takahashi, T., (2007), Debris Flows: mechanics, prediction and countermeasures. Balkema, Rotterdam.

[2] O'Brien, J.S. and Julien, P.Y. (1988), "Laboratory analysis of mudflow properties.", Journal of Hydraulic Engineering, Vol.114, No.8, p.877-887.

[3] Bagnold, R. A. (1954), "Experiments on a gravity-free dispersion of large solid spheres in a Newtonian fluid under shear." Proceedings of the Royal Society of London. Series A, Mathematical and Physical Sciences, Vol.225, No.1160, p.49-63.

[4] Bisantino T., Fischer P., Gentile F., "Rheological characteristics of debris-flow material in south Gurgaon watersheds" [J].Natural Hazards, 2009, 54(2):209 -233.

[5] Lin, F., et al. (2021). "3D in-situ simulation and particle tracing of gas filtration process for ultrafine particles removal using a hollow fiber membrane." Journal of Membrane Science 632.

[6] Wei-Ming Lu, Kuo-Lun Tung , Kuo-Jen Hwang, "Effect of woven structure on transient characteristics of cake filtration",Chemical Engineering, Volume 52, Issue 11,1997,Pages 1743-1756

[7] Comsol：Flow of Viscoelasic Fluid Past Cylinder, (2012).

[8] Comsol：Inkjet Nozzle-Level Set,(2012)

[9] Comsol : rising bubble modeled with the level set method, (2012).

[10] Jan,C,-D,and H.W.Shen(1997) Review dynamic modeling of debris flows. Recent Developments on Debris Flows:93-116.

[11] Hang,M,et al(2023). "Shear behavior of-order morphology in rock joints."Journal of Mountain Science 20(3):845-858.

[12] Johnson, A. M. and Rodine, J. R. (1984), "Slope Instability – Debris flow" John Wiley and Son, Edited by Brunsden, D. and Prior, D. B., p.257-361.

[13] Comsol: CFD Module Users Guide, (2012).

[14] Tecca,, P.R., Galgaro, A., Genevois, R., and Deganutti, A.M.(2003), "Development of a remotely controlled debris flow monitoring system in the Dolomites (Acquabona, Italy) ," Hydrol. Process., Vol. 17, p.1771-1784

[15] Rickenmann, D., Laigle, D., McArdell, B.W., Hübl. J. (2006a): Comparison of 2D debris-flow simulation models with field events. Computational Geosciences, 10: 241–264, DOI: 10.1007/s10596-005-9021-3

[16] Naef, D., Rickenmann, D., Rutschmann, P., McArdell, B.W. (2006b): Comparison of flow resistance relations for debris flows using a one-dimensional finite element simulation model. Natural Hazards and Earth System Sciences, 6: 155-165.

[17] Jan, C. D. and H.W. Shen (1997), "Review Dynamic Modeling of Debris Flows." Lecture Notes in Earth Sciences, Vol. 64, pp. 93-116.
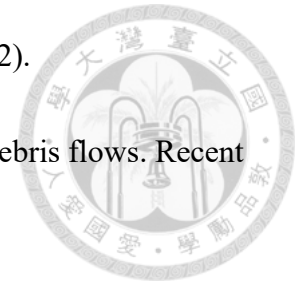
[18] Weclas, M., Melling, A., and Durst, F., 1998, "Flow Separation in the Inlet Valve Gap of Piston Engines," Prog. Energy Combust. Sci., 24(3), pp. 165–195.
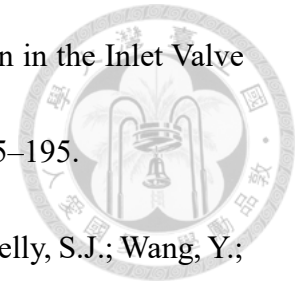
[19] . Kioumourtzoglou, M.A.; Schwartz, J.D.; Weisskopf, M.G.; Melly, S.J.; Wang, Y.; Dominici, F.; Zanobetti, A. Long-term PM2.5 Exposure and Neurological Hospital Admissions in the Northeastern United States. Env. Health Perspect 2016, 124, 23–29.

[20] Wang, Y.; Wang, Y.; Liu, W.; Chen, D.; Wu, C.; Xie, J. An aerosol sensor for PM1 concentration detection based on 3D printed virtual impactor and SAW sensor. Sens. Actuators A Phys. 2019, 288, 67–74

[21] Auton, T.R., Hunt, J.C.R., Prud'homme, M., 1988. The force exerted on a body in inviscid unsteady non-uniform rotational flow. J. Fluid Mech. 197, 241-257.

[22] Andrews, M.J. and O'Rourke, P.J., 1996. The multiphase particle-in-cell (MP-PIC) method for dense particle flow. Int. J. Multiphase Flow 22, 379.

[23] Apte, S.V., Mahesh, K., Lundgren, T., 2008. Accounting for finite-size effects in simulations of disperse particle-laden flows. Int. J. Multiphase Flow 34, 260-271.

Bradley, W.H., 1965. Vertical density currents. Science 150, 1423-1428.

[24] Batchelor, G.K., 1967. An introduction to fluid dynamics, Cambridge University Press. Pages 230-235.
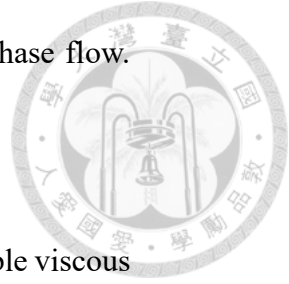
[25] Balachandar, S., Eaton, J.K., 2010. Turbulent dipersed multiphase flow. Annual Reviewof Fluid Mechanics 42, 111-133.

[26] Chorin A.J., 1967 A numerical method for solving incompressible viscous flow problems. J. Comput. Phys. 2, 12-26.

[27] Cui, A., Street, R.L., 2001. Large-eddy simulation of turbulent rotating convective flow development. J. Fluid Mech. 447, 53-84.

[28] Chou, Y.-J., Wu, F.-C., Shih, W.-R., 2014. Toward numerical modeling of fine particle suspension using a two-way coupled Euler–Euler model: Part 1: Formualtion and comparison to single-phase approximation. Int. J. Multiphase Flow 64, 35-43.

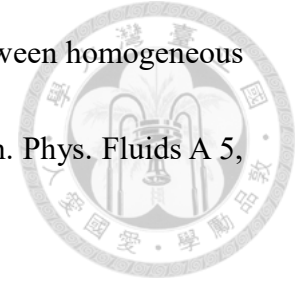[29] Chou, Y.-J., Wu, F.-C., Shih, W.-R., 2014. Toward numerical modeling of fine particle suspension using a two-way coupled Euler–Euler model: Part 2: Simulation of particle-induced Rayleigh–Taylor instability. Int. J. Multiphase Flow 64, 44-54.

[30] Drew, D.A., Passman, S.L., 1998. Theory of Multicomonent Fluids. Springer-Verlag, New Yo

Elghobashi S, Truesdell GC. 1993. On the two-way interaction between homogeneous turbulence and dispersed solid particles. I: Turbulence modification. Phys. Fluids A 5, 1790-801.

[31] Eaton JK. 2009. Two-way coupled turbulence simulations of gas-particle flows using point particle tracking. Int. J. Multiphase Flow 35, 792-800.

[32] Ferry, J., Balachandar, S., 2001. A fast Eulerian method for disperse two-phase flow. Int. J. Multiphase Flow 27, 1199-1226.

[33] Ferrante A, Elghobashi S. 2003. On the physical mechanism of two-way coupling in particle-laden isotropic turbulence. Phys. Fluids 15, 315-29.

[34] Harlow, F.H., Amsden, A.A., 1971. Fluid Dynamics, A LASL Monograph, LA-4700 (Los Alamos National Laboratories, Los Alamos, NM, 1971).

[35] Maxey, M.R., Riley, J.J., 1983. Equation of motion for a small rigid sphere in a nonuniform flow. Physics of Fluids 26, 883-889.

[36] Patankar, N.A., Joseph, D.D., 2001b. Lagrangian numerical simulation of particulate flows. Int. J. Multiphase Flow 27, 1685-1706.

[37] Snider, D.M., 2001. An incompressible three-dimensional multiphase particle-in-cell model for dense particle flows. J. Comput. Phys. 170, 523-549.

[38] van der Hoef, M.A., van Sint Annaland, M., Deen, N.G., Kuipers, J.A.M., 2008.

Numerical simulation of dense gas-solid fluidized beds:a multiscale modeling strategy.

Annual Review of Fluid Mechanics 40, 47-70.